Delft University of Technology

Thermodynamic modeling of alkali-activated fly ash paste

Chen, Yun; Ma, Bin; Chen, Jiayi; Li, Zhenming; Liang, Xuhui; de Lima, Luiz Miranda; Liu, Chen; Yin, Suhong; Yu, Qijun; Lothenbach, Barbara

DOI
10.1016/j.cemconres.2024.107699

Publication date
2024

Document Version
Final published version

Published in
Cement and Concrete Research

Citation (APA)
Chen, Y., Ma, B., Chen, J., Li, Z., Liang, X., de Lima, L. M., Liu, C., Yin, S., Yu, Q., Lothenbach, B., & Ye, G. (2024). Thermodynamic modeling of alkali-activated fly ash paste. *Cement and Concrete Research*, *186*, Article 107699. https://doi.org/10.1016/j.cemconres.2024.107699

Important note
To cite this publication, please use the final published version (if applicable).
Please check the document version above.

Copyright
Other than for strictly personal use, it is not permitted to download, forward or distribute the text or part of it, without the consent of the author(s) and/or copyright holder(s), unless the work is under an open content license such as Creative Commons.

Takedown policy
Please contact us and provide details if you believe this document breaches copyrights.
We will remove access to the work immediately and investigate your claim.

This work is downloaded from Delft University of Technology.
For technical reasons the number of authors shown on this cover page is limited to a maximum of 10.

Cement and Concrete Research 186 (2024) 107699

Contents lists available at ScienceDirect

Cement and Concrete Research

journal homepage: www.elsevier.com/locate/cemconres

Thermodynamic modeling of alkali-activated fly ash paste

Yun Chen [a,b], Bin Ma [c], Jiayi Chen [a], Zhenming Li [d,e], Xuhui Liang [a], Luiz Miranda de Lima [a], Chen Liu [a], Suhong Yin [b], Qijun Yu [b], Barbara Lothenbach [f,*], Guang Ye [a,*]

[a] Section of Materials and Environment, Faculty of Civil Engineering and Geosciences, Delft University of Technology, Delft 2628CN, the Netherlands
[b] School of Materials Science and Engineering, South China University of Technology, Guangzhou 510640, Guangdong, China
[c] College of Environmental Science and Engineering, North China Electric Power University, Beijing 102206, China
[d] School of Civil and Environmental Engineering, Harbin Institute of Technology, 518055 Shenzhen, China
[e] Guangdong Provincial Key Laboratory of Intelligent and Resilient Structures for Civil Engineering, Harbin Institute of Technology, 518055 Shenzhen, China
[f] Concrete & Asphalt Laboratory, Swiss Federal Laboratories for Materials Science and Technology (Empa), Dübendorf 8600, Switzerland

ARTICLE INFO

Keywords:
Alkali-activated fly ash
Reaction kinetics
Thermodynamic modeling
Image analysis
Pore solution

ABSTRACT

Previously, the lack of a thermodynamic database for N-(C-)A-S-H gel limited the application of thermodynamic modeling to alkali-activated fly ash (AAFA). This study pioneers thermodynamic modeling of AAFA using a recently developed thermodynamic dataset for N-(C-)A-S-H gel. The reaction products, pore solutions and reaction kinetics of AAFA pastes were experimentally determined. Based on the reaction kinetics, the composition of the solid phases and the pore solution of AAFA were modeled over time. The results showed that the simulated compositions of the solid reaction products and pore solution match closely with the experimental results, especially for the sodium hydroxide-activated system. Moreover, modeling results point out the potential presence of minor reaction products (e.g., C-(N-)A-S-H gel, microcrystalline ferrihydrite, Mg-containing phases) undetectable by experimental techniques. The study also demonstrated that thermodynamic modeling accurately captured the amount of bound water in reaction products, highlighting its robustness in both qualitative and quantitative analysis.

1. Introduction

Alkali-activated fly ash (AAFA) is a sustainable, cement-free binder that forms through the reaction of fly ash with alkaline activator(s). Properly mixed and cured, AAFA can surpass Portland cement in various engineering aspects, including achieving higher mechanical strength [1,2], exhibiting greater chemical resistance [3,4], demonstrating lower shrinkage [5] and providing better thermal resistance [6,7]. The reactions of AAFA are influenced by several factors such as the properties of fly ash, the types and concentrations of alkaline activators and the curing regime. As a result, the microstructure of AAFA varies significantly, leading to a wide range of engineering properties. Accurately predicting the reaction is crucial for designing AAFA with desired properties.

Thermodynamic modeling, a theoretically rigorous and computationally efficient tool, is widely used for predicting chemical reactions under equilibrium conditions. This approach has been extensively applied for cement and alkali-activated slag (AAS) systems using the Cemdata18 thermodynamic database [8–10]. However, thermodynamic modeling of AAFA has rarely been reported due to the absence of thermodynamic data for N-A-S-H gel, the primary reaction product of AAFA. A few studies used either estimated data or data of crystalline zeolites to describe N-A-S-H gel [10–12]. Despite sharing a similar composition with zeolites, N-A-S-H gels are significantly more soluble and diverge in structure. Such differences in stability can affect the accuracy and reliability of modeling outcomes.

In our previous study [13], thermodynamic data of N-A-S-H gels with varying Si/Al ratios (1 to 3) has been determined, enabling the accurate thermodynamic modeling of AAFA using appropriate solubility data. However, it is important to note that calcium (Ca) can also be incorporated into N-A-S-H gel to form low-Ca N-C-A-S-H gel [14]. Although N-C-A-S-H gel often appears in AAFA systems blended with small amounts of slag or cement [14–17], it is also likely to form in the AAFA system due to the minor amounts of Ca typically present in fly ash. Thus, addressing the incorporation of Ca into N-A-S-H gel is a prerequisite for thermodynamic modeling of AAFA.

Accurately predicting chemical reactions over time requires the consideration of reaction kinetics alongside thermodynamic modeling

---

* Corresponding authors.
E-mail addresses: barbara.lothenbach@empa.ch (B. Lothenbach), G.Ye@tudelft.nl (G. Ye).

https://doi.org/10.1016/j.cemconres.2024.107699
Received 29 May 2024; Received in revised form 28 August 2024; Accepted 10 October 2024
Available online 22 October 2024
0008-8846/© 2024 The Authors. Published by Elsevier Ltd. This is an open access article under the CC BY license (http://creativecommons.org/licenses/by/4.0/).

[18]. This combined approach, previously applied to AAS [12,19], faces challenges in AAFA due to the difficulty in determining the reaction degree of fly ash. So far, selective dissolution and backscattered electron (BSE) image analysis are the most common methods to determine the reaction degree of fly ash [20–23]. Selective dissolution, though commonly employed, introduces considerable uncertainty. This arises from the possibility of dissolving small fractions of fly ash, while specific reaction products, particularly those containing magnesium, remain undissolved regardless of the solvent used. On the other hand, BSE image analysis relies on precise segmentation to distinguish unreacted fly ash from the matrix. However, the similarity in grey levels between the unreacted fly ash and reaction products presents a notable challenge in accurately segmenting different phases and can lead to significant systematic errors. Therefore, developing more accurate methods to assess the reaction degree of fly ash in AAFA is essential for a realistic evaluation of reaction kinetics.

The aim of this study is to fill the gap in the thermodynamic modeling of AAFA using a recently developed thermodynamic dataset for N-(C-)A-S-H gel. This study is structured into three parts, as outlined in Fig. 1. The first segment involves the characterization of AAFA paste in terms of its solid and aqueous phases. The reaction products and microstructure of AAFA paste are investigated by using X-ray diffraction (XRD), Fourier transform infrared (FTIR) spectrometry, thermogravimetric analysis (TGA) and scanning electron microscopy/energy dispersive spectroscopy (SEM-EDS) techniques. The ion concentrations in the pore solution of AAFA are quantified by titration and inductively coupled plasma-optical emission spectroscopy (ICP-OES) analysis. These results are used to guide and validate the thermodynamic modeling results. The reaction degree of fly ash is determined via image analysis, which is then combined with isothermal calorimetry data to refine the reaction kinetics in the second segment. The reaction kinetics provides the kinetic input for thermodynamic modeling in the third segment. To perform thermodynamic modeling of AAFA, N-C-A-S-H gels are synthesized and their thermodynamic data are determined. By combining the thermodynamic data of N-A-S-H gel determined in [13] with the data gained here, a thermodynamic database of N-(C-)A-S-H[1] gels with various Si/Al and Ca/Al ratios is established. Thermodynamic modeling of AAFA reaction is performed with the GEMS software to simulate the evolution of solid and aqueous phases, which are also compared against experimental data for validation. The outcome of this study highlights the potential of thermodynamic modeling to evaluate the effect of different influencing factors on AAFA reactions, thereby helping to tailor the mix design of AAFA systems with desired properties.

2. Experimental methods

2.1. Raw materials and mixtures

The chemical composition of fly ash, as determined by X-ray fluorescence spectroscopy (XRF), and its mineral components identified by quantitative XRD analysis (QXRD), are listed in Table 1. The amorphous content of fly ash was 79 wt% based on QXRD. It is assumed that only the amorphous phase in fly ash is reactive, while the crystals are considered non-reactive. Based on the content of crystalline SiO_2 and Al_2O_3 from QXRD results, the reactive SiO_2 and Al_2O_3 were determined as 44 wt% and 18 wt%, respectively. According to the definition in [24], the fly ash used in this study can be classified into Class F. The density of fly ash is 2.13 g/cm^3. The particle size distribution (PSD) of fly ash, as measured using laser diffraction, indicates a d_{50} of the fly ash of 43 μm (see Fig. A1).

Sodium hydroxide (NH) activated and sodium silicate (NS) activated systems were chosen for the investigation of AAFA paste. The alkali activators were prepared by sodium hydroxide (>98 wt%) pellets, sodium silicate solution (27.5 wt% SiO_2, 8.25 wt% Na_2O and 64.25 wt% H_2O) and deionized water. For NH-activated system, the Na_2O content in the activator was 9.3 wt%. The modulus Ms. (molar ratio SiO_2/Na_2O) of the activator was 0. The water-to-fly ash ratio was 0.35. For NS-activated system, the same Na_2O dosage and water-to-fly ash ratio were used, but with a SiO_2/Na_2O modulus of 1. All samples were cured in a sealed condition at 40 °C until the age of testing.

2.2. Characterization of AAFA paste

2.2.1. Reaction products

In order to explore the components of AAFA paste, the samples cured after 7 days and 28 days were subjected to XRD, FTIR, TGA and SEM-EDS analysis. Prior to XRD, FTIR, TGA measurements, the samples were ground to powder in isopropanol to halt any ongoing reactions. Detailed procedures were described in [25]. For SEM-EDS analysis, the samples were sectioned into about 1 cm thick slices and immersed in isopropanol for 2 weeks to stop reactions. Isopropanol was renewed 3 times in the first week. Subsequently, samples were dried at 25 °C in a vacuum oven for around 1 week.

2.2.1.1. XRD analysis. XRD analysis was carried out on both the raw fly ash and powdered paste using a Bruker D8 Advance diffractometer at 45 KV and 40 mA using CuKα radiation. The powdered samples were scanned from 5° to 90° 2θ at a rate of 2 s per step and a step size of 0.02° 2θ. In order to measure the quantities of different phases in fly ash and paste, 10 wt% of silicon powder was used as an internal standard. The Rietveld quantitative analysis was performed in the software Profex-BGMN [26] to determine the amounts of each phase.

2.2.1.2. FTIR analysis. To further analyze the phase in AAFA paste, FTIR measurement was conducted on raw fly ash and powdered paste using Nicolet™ iS50 FTIR Spectrometer over the wavelength range of 400 to 4000 cm^{-1} with a resolution of 4 cm^{-1}. A total of 32 scans were collected per measurement.

2.2.1.3. TGA. TG measurement was carried out on around 20 mg of powders at a heating rate of 10 °C/min from 40 °C to 1000 °C with a thermoanalyzer TG-449-F3-Jupiter instrument. The mass loss of the first peak (80–270 °C) was used to evaluate the amount of physically and chemically bound water in the reaction products.

2.2.1.4. SEM-EDS analysis. Before performing SEM-EDS, the samples were impregnated with epoxy, allowed to harden and then polished with successively finer grades of silicon carbide papers and polishing discs [27]. After that, the samples were sputter coated with carbon and then examined by a FEI QUANTA FEG 650 ESEM equipped with a solid-state EDS detector in backscattered electron (BSE) mode. The working distance was set as 10 mm. The accelerating voltage used was 15 kV [23,28,29], as an optimal choice between consideration of spatial resolution, interaction volume and adequate excitation of the FeKα peak [30].

The images and EDS maps were collected with a magnification of 1000×, a resolution of 1024*682 and a pixel size of 0.4 μm. The spectral images were obtained using a dwell time of 143 μs per pixel over 20 frames. The total acquisition time of a map is 2000s. Phase segmentation was carried out on 15–20 maps by image analysis to further analyze microstructure and determine degree of reaction of fly ash.

2.2.1.5. Segmentation of BSE image. As observed in previous studies [28,31], the grey levels of reaction products and most unreacted fly ash are similar, posing challenges in phase segmentation. An optimized method is proposed in this work to distinguish fly ash and reaction products, moving beyond the reliance solely on grey level histograms. Each image was segmented into three phases, i.e. fly ash, reaction

---

[1] N-(C-)A-S-H in this study refers to both N-A-S-H and N-C-A-S-H gels.

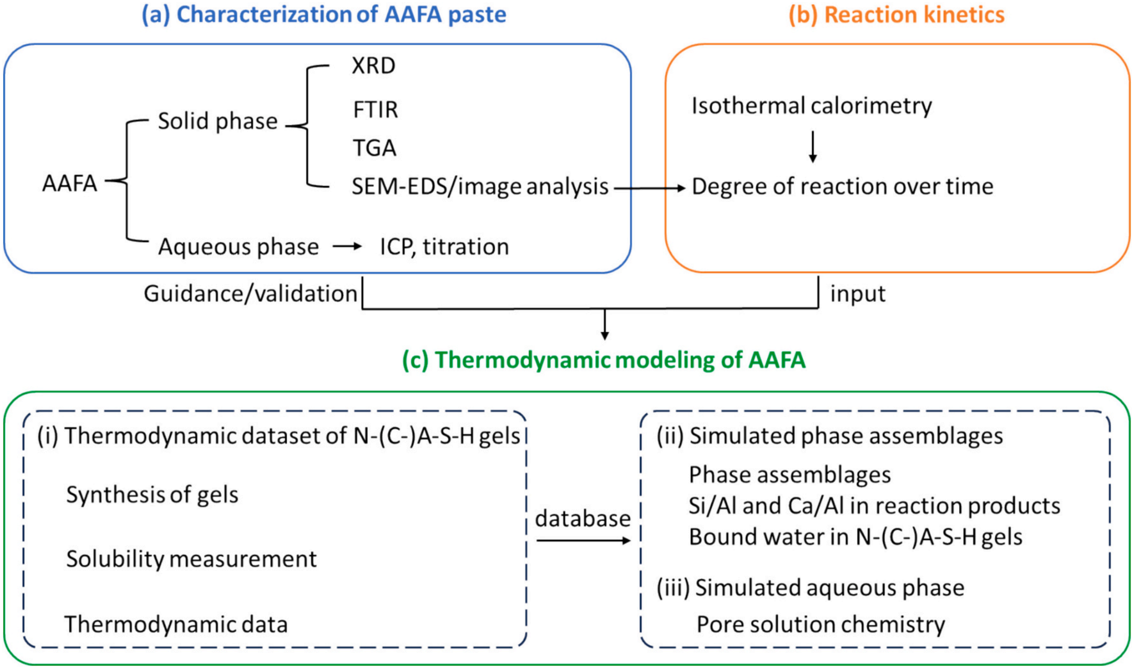

Fig. 1. The structure of this study.

Table 1
Chemical compositions and components of fly ash (by wt%).

Oxides	SiO_2	Al_2O_3	Fe_2O_3	CaO	MgO	K_2O	Na_2O	P_2O_5	TiO_2	SO_3	LOI
	56.75	24.58	5.76	3.93	2.10	1.40	1.27	1.17	1.03	0.68	1.33
Components	Amorphous phase			Quartz		Mullite		Maghemite		Calcite	
	79.3			10.1		9.6		0.7		0.3	

LOI: loss on ignition.

products and voids, by using Otsu's method [32], which automatically finds the thresholds based on atomic counts and grey level. The detailed conditions for segmentation can be found in Fig. A2. Since the epoxy contains a little Cl, only the regions devoid of Cl were further taken into consideration. Notably, due to a noticeable disparity in Na content between fly ash and other phases, regions lacking Na and exhibiting a low grey level were designated as fly ash. Additionally, dark regions lacking Na but containing Fe were also classified as fly ash, considering some Fe-containing fly ash particles displayed high grey level values. In contrast, regions containing Na while simultaneously displaying a low grey level were categorized as reaction products. Any region that did not meet the criteria for fly ash or reaction products was identified as voids. Note that the final phase segmentation of AAFA is shown in the Section 3.1.4.

2.2.2. *Pore solution*

To analyze the aqueous concentrations, pore solutions of the pastes at curing age of 7 and 28 days were extracted following the method depicted in [33]. The cylinder paste with a diameter of about 34 mm and a height of about 70 mm was inserted into the hollow steel cylinder with a fitting size of the paste. A maximum force of 300–600 kN, depending on the type and reaction degree of the pastes, was applied to extract the pore solutions [34]. For each sample, around 0.5–2 mL of pore solution was collected. Directly after extraction, the pore solution was filtred using a 0.45 μm syringe filter. The OH^- concentration of the pore solution was immediately measured by titration with 0.1 M HCl standard solution against phenolphthalein. The concentrations of Si, Al, Na, Ca, Fe, Mg and K were determined by a Perkin Elmer Optima 5300 DV ICP-OES spectrometer after dilution with nitric acid (0.2 vol%).

2.2.3. *Degree of reaction of fly ash*

The degree of reaction of fly ash at certain curing ages was determined by image analysis as described in Section 2.2.1. Previous study [35] has already shown that the area fraction in two dimensions can be reasonably equated to the volume fraction in three dimensions. Thus, the area fraction of fly ash derived from image analysis was used to calculate the degree of reaction by using the following equation:

$$\alpha(t) = (1 - F_t/F_0)*100\% \tag{1}$$

where $\alpha(t)$ is the degree of reaction of fly ash at age t, F_t is the volume fraction of fly ash at age t, and F_0 is the initial volume fraction of fly ash, as done in several studies [23,36,37].

2.2.4. *Reaction kinetics*

To obtain the continuous reaction degree as a function of time (reaction kinetics), a linear proportionality between reaction degree and heat release is assumed according to Eq. (2) [12,37]. To measure the heat release, in-situ isothermal calorimetry tests were performed by using a TAM-Air-314 isothermal calorimeter at 40 °C. Calibration was carried out before each measurement. Around 4 g of fly ash were loaded in the glass ampoule, while the activator solution was stored in an attached syringe. The admix ampoule was placed in the calorimeter for around 3 h to reach a stable heat flow baseline. After that, the activator solution was injected into the glass ampoule and mixed with fly ash using a built-in stirring shaft. Heat flow was recorded until 7 days. The calorimetry results were normalized by the mass of fly ash.

Based on the degree of reaction at 7 days determined by image analysis and the cumulative heat release of the AAFA paste at 7 days, the maximum heat release (Q_{max}) can be calculated using Eq. (2). Since the cumulative heat release obtained from experiment was only available up to 7 days, $Q(t)$ was fitted by using the Eq. (3) [38] to describe the cumulative heat release over extended time. Consequently, the continuous reaction degree of fly ash as a function of time can be calculated with the Eq. (4). It should be noted that the parameter Q_{max} in Eq. (4) cannot be simply interchanged with the fitting maximum heat release Q_{max_fit}. As outlined in [12,39], Q_{max_fit} obtained from the Eq. (3) tends to be underestimated significantly, resulting in an overestimation of reaction degree. Hence, it is essential to derive Q_{max} from experimental result ($\alpha(t)$) using Eq. (2).

$$\alpha(7d) = Q(7d)/Q_{max} \tag{2}$$

$$Q\ (t) = Q_{max\_fit} exp\left(-\left(\frac{\lambda}{t}\right)^{\beta}\right) \tag{3}$$

$$\alpha(t) = Q_{max\_fit} exp\left(-\left(\frac{\lambda}{t}\right)^{\beta}\right)/Q_{max} \tag{4}$$

Note that the maximum heat release (Q_{max}) calculated in this study assumes that 100% of the fly ash, including both amorphous and crystalline fly ash, reacts, which is unlikely to happen in reality. However, although the calculated Q_{max} is unattainable, using Eq. (2) for this calculation ensures that the reaction degree derived from Eq. (4) remains consistent and reasonable, given that the reaction degree of fly ash will not reach 100% in reality either.

2.3. *Thermodynamic modeling*

2.3.1. *Thermodynamic data of N-C-A-S-H gels*

To perform thermodynamic modeling of AAFA, the thermodynamic data of N-A-S-H gels determined in our previous work [13] was used and completed with the thermodynamic data of N-C-A-S-H gels determined here. The determination of thermodynamic data of N-C-A-S-H gels in this work followed the same approach applied to determine that of N-A-S-H gels in [13]. Firstly, four types of N-C-A-S-H gels with various Si/Al and Ca/Al ratios were synthesized via the sol-gel method as described in detail in the Appendix (refer to Tables A1, A2 and Figs. A3, A4). The obtained N-C-A-S-H gels were subjected to a dissolution test at 25 °C using a water-to-solid ratio of 20 g/L until equilibrium was reached after 60 days. The total concentrations of Na, Ca, Al and Si in the filtrated solution as well as the pH values were used to calculate the solubility products of the different N-C-A-S-H gels, as shown in Table A4. The Gibbs free energy of formation $\Delta_f G^0$ was calculated from the derived solubility products, heat capacity C_p^0 and entropy S^0 were estimated as described in [13] and used to also derive the enthalpy of formation $\Delta_f H^0$. Consequently, a thermodynamic database of N-(C-)A-S-H gels was developed by incorporating the thermodynamic properties of three types of N-A-S-H gels and four types of N-C-A-S-H gels.

2.3.2. *Thermodynamic modeling of AAFA*

The thermodynamic modeling of AAFA paste was performed in GEMS at 40 °C. The PSI/Nagra [40] and Cemdata18 [8] thermodynamic databases were used as the basis databases to describe the thermodynamic data for general solid, aqueous, and gaseous phases. In addition, thermodynamic data of N-(C-)A-S-H gel ([13], and derived here) and zeolites [41] were also added to describe the reaction products of AAFA materials.

The built-in extended Debye-Huckel equation was used to compute the activity coefficients of the aqueous species. It should be noted that this equation is thought to be applicable up to 1–2 M ionic strength [42,43], while AAFA pore solutions can have inititally a higher ionic strength (referring to 1–3 M in AAS system [44]). It has been shown that the modeling results obtained from the extended Debye-Huckel equation used here and the Pitzer model (more suitable for higher ionic strength) are comparable in alkali-activated systems, especially at later ages [12].

The components in the amorphous fly ash considered in the thermodynamic modeling include SiO_2, Al_2O_3, Fe_2O_3, CaO, MgO, Na_2O and K_2O, while the others were omitted due to their minimal quantities. These amorphous oxides are assumed to dissolve congruently in thermodynamic modeling, whereas the crystalline phases are considered to be inert.

The formation of zeolites was partly suppressed during the thermodynamic modeling to prevent the thermodynamically more stable zeolites forming instead of the observed N-(C-)A-S-H gel, as the formation of zeolites is often kinetically hindered while N-(C-)A-S-H gel precipitate instead [13]. The suppression of zeolites is based on the QXRD results of AAFA paste. In NH-activated system, the formation of hydroxysodalite (SOD(OH)) was observed, approximately 3% regardless of curing age. Consequently, the upper limit for the quantity of hydroxysodalite was set at 0.005 M (4.84 g) for 100 g of fly ash, while other zeolites were suppressed. In NS-activated system, all zeolites are inhibited as no crystalline zeolite phase was observed. The formation of hematite, magnetite and goethite was also prevented due to the kinetic reason.

The amount of bound water (m_{H_2O}) in the modeled solid phases was estimated using the following equation:

$$m_{H_2O} = w_{\mathrm{N(C)ASH}} \bullet m_{\mathrm{N(C)ASH}} + w_{\mathrm{C(N)ASH}} \bullet m_{\mathrm{C(N)ASH}} + w_{MSH} \bullet m_{MSH} \tag{5}$$

where $m_{\mathrm{N(C)ASH}}$, $m_{\mathrm{C(N)ASH}}$ and m_{MSH} are the mass of the modeled N-(C-)A-S-H gel, C-(N-)A-S-H gel and magnesium silicate hydrates (MSH), respectively. w refers to the fraction of bound water in these solid phases. $w_{\mathrm{N(C)ASH}}$=20% (see Fig. A1 and refs [13, 45]); $w_{\mathrm{C(N)ASH}}$= 25% [45]; w_{MSH}=15% [46,47].

3. Results and discussion

3.1. *Solid and aqueous phases characterization*

3.1.1. *XRD analysis*

The XRD patterns of the unreacted fly ash and AAFA pastes cured for 7 days and 28 days are shown in Fig. 2. In addition to the amorphous phase, fly ash also contains crystalline phases such as quartz, mullite and magnetite. These crystalline phases are also visible in the XRD patterns of AAFA pastes, as those phases are not-reactive and hardly dissolved. The main reaction product of AAFA is an amorphous gel (i.e. N-(C-)A-S-H gel), as evidenced by the broad hump at 20–40° 2θ [48,49]. In addition, hydroxysodalite ($Na_8Al_6Si_6O_{24}(OH)_2{\cdot}2H_2O$) was found in the NH-activated system, while no zeolitic phase was formed in the NS-activated system. This finding is consistent with previous observations [49,50], which also observed that hydroxysodalite is formed in low SiO_2 environments. In addition, a small peak located at around 29° 2θ was found in the NH-activated system but absent in the NS-activated system.

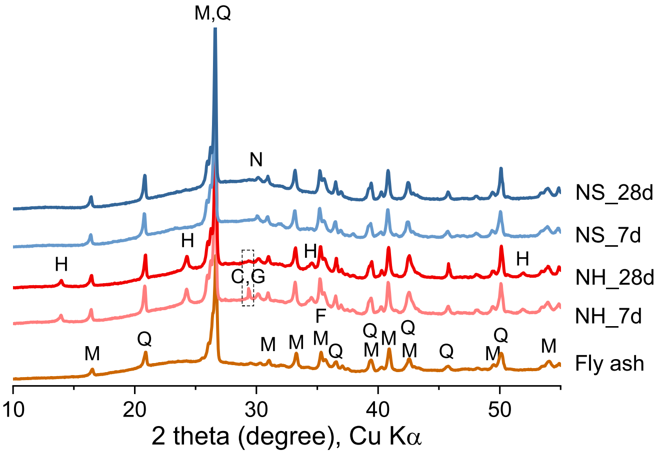

Fig. 2. XRD patterns of fly ash and the NaOH (NH) and Na-silicate (NS) activated AAFA pastes cured at 40 °C. H: hydroxysodalite; M: mullite; Q: quartz; N: natrite; G: C-(N-)A-S-H gel; C: calcite; F: magnetite.

Although calcite is mainly responsible for this peak, it should be noted that the peak of C-(N-)A-S-H gel is also located at this position [51,52]. The potential existence of C-(N-)A-S-H gel will be further discussed based on the FTIR results given below and in the thermodynamic modeling section.

3.1.2. FTIR analysis

FTIR analysis was conducted on both the unreacted fly ash and the AAFA pastes, see Fig. 3. The quartz in fly ash results in a series of bands at around 1150, 1084, 796–778 (double band), 697, 668, 522 and 460 cm^{-1} [53]. The mullite can contribute to the bands at around 1180–1130 cm^{-1} and 560–550 cm^{-1}, while the amorphous phase in fly ashes typically shows a band around 996 cm^{-1} [54]. These phase-induced bands overlap, thus giving rise to an IR spectrum for fly ash marked by a primary broad band between 1250 and 850 cm^{-1}, a dual-band at 795–777 cm^{-1}, a minor band at 560 cm^{-1}, and a robust band at 463 cm^{-1}.

Compared to unreacted fly ash, the main band of AAFA pastes exhibited varying degrees of wavenumber shift towards lower values. A newly emerged signal, centered at around 969–997 cm^{-1}, is attributed to the main reaction product, i.e. N-(C-)A-S-H gel [54,55]. The location of this band, corresponding to the asymmetric stretching vibrations of Si-O-T bonds, indicates the polymerization level of the N-(C-)A-S-H gel. A higher wavenumber of this band is observed with an increase in reaction time, signifying the formation of a more polymerized N-(C-)A-S-H gel. Furthermore, this band is observed at higher wavenumbers in the NS-activated system than the NH-activated system, mainly due to the higher Si/Al ratio of N-(C-)A-S-H gel formed in the NS-activated system. This agrees with the observation in [13] that the wavenumber of the Si-O-T asymmetric stretching band in N-(C-)A-S-H gel increases with the Si/Al ratio. Also low Ca/Si C-(A-)S-H phases have their main band at around 960 cm^{-1} [56–58], which could also contribute to the observed signal. The sharp band at 969 cm^{-1} for sample NH-7d would also be another support for the formation of C-(N-)A-S-H gel in the NH-activated system. A small band at around 1170 cm^{-1}, contributed by Q^4 [55], is presented in the NS-activated system. Two weak bands at 694 and 662 cm^{-1}, as highlighted by the black dashed rectangle, are observed in the NH-activated system, but hardly in the NS-activated system. Both bands arise from the formation of hydroxysodalite [41,59], which aligns with the XRD result.

The band at 463 cm^{-1} observed in the unreacted fly ash corresponds to internal bending vibrations of the O-T-O groups (T refers to Si or Al) [41,55]. This band shifts to lower wavenumber after activation, in particular for the NH-activated system, which is attributed to the lower wavenumber of O-Al-O bending vibration compared to that of O-Si-O bending vibration [55]. This result also implies that the reaction product in the NH-activated system has a lower Si/Al ratio than that in the NS-activated system. Furthermore, the newly emerged band at near 1643 cm^{-1} is assigned to the bending vibration of H-O-H bond [59,60]. The small peak at around 1436–1446 cm^{-1}, characteristic of asymmetric stretching vibrations of C-O bond, indicates that some samples were slightly carbonated [61,62].

3.1.3. TGA

The thermogravimetric (TG) and differential thermogravimetric (DTG) analysis are shown in Fig. 4. All samples present a pronounced mass loss ranging from 6 to 8 wt% within the range of 80–270 °C, which is mainly attributed to the dehydroxylation of N-(C-)A-S-H gel [63]. The NS-activated system shows a more substantial mass loss compared with NH-activated system, implying the formation of a higher quantity of N-(C-)A-S-H gel. Moreover, the temperature at the peak of this mass loss (marked by the dashed line and arrow) increases with longer curing times. The temperature of this peak is also higher in the NS-activated system than in the NH-activated system. The shift suggests a stronger binding of water within the gel structure [16,64,65]. From 250 to 1000 °C a more gradual mass loss can be observed across all samples, which could be associated with the dehydroxylation of silanol groups [66], burning of carbon in the fly ash [67] or the decomposition of carbonates [68]. A slight mass loss at around 840 °C is observed in the NH-activated system, which is related to dehydroxylation of hydroxysodalite [69].

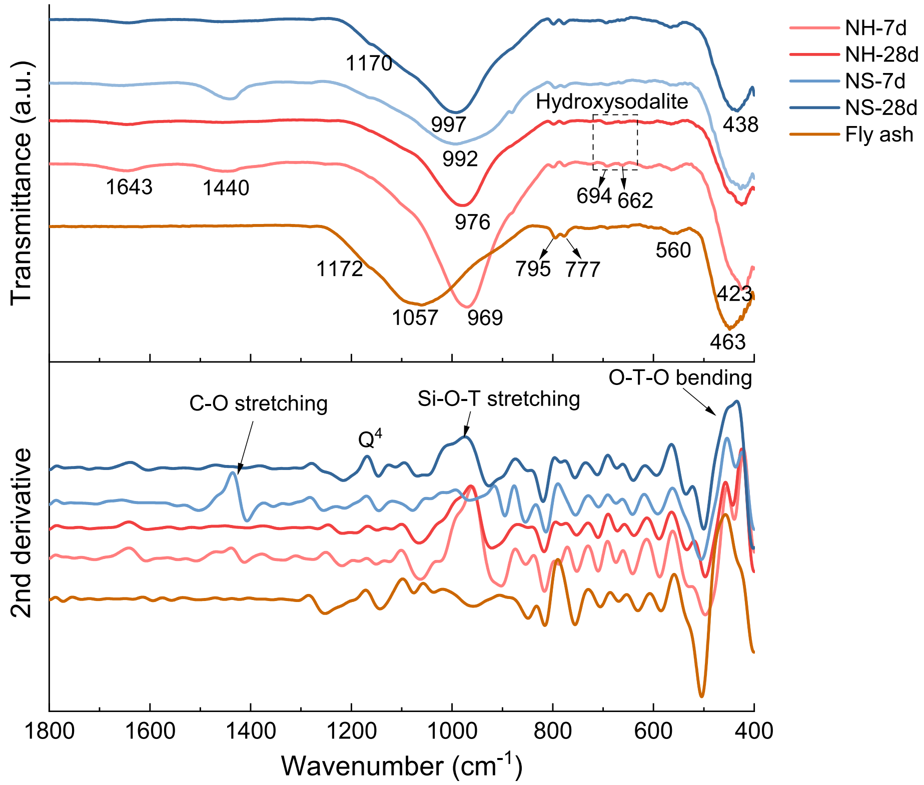

Fig. 3. FTIR curves of the unreacted fly ash, NaOH (NH) and Na-silicate (NS) activated fly ash pastes cured at 40 °C.

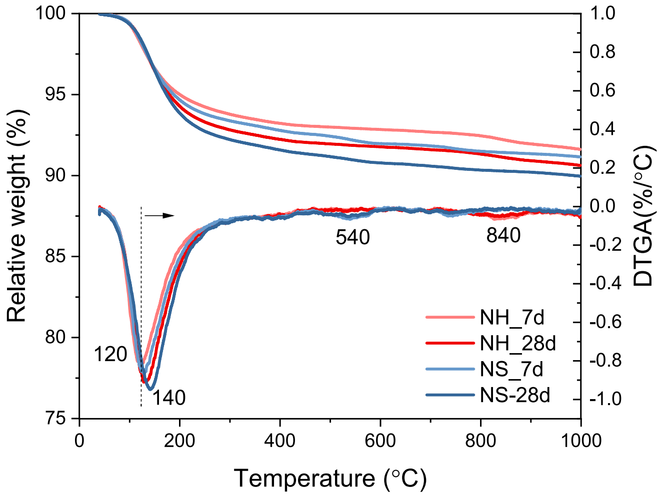

Fig. 4. TG-DTG curves of the NaOH (NH) and Na-silicate (NS) activated fly ash pastes cured at 40 °C.

3.1.4. SEM-EDS analysis

The information obtained from SEM-EDS for samples at 28 days is shown in Fig. 5, with corresponding information for samples at 7 days provided in Appendix (Fig. A3). Microstructures of the hardened AAFA pastes at 28 days can be observed in Fig. 5 (a). In accordance with the observations of [48,70], the NH-activated system displayed a loose and porous microstructure, while a denser and homogeneous microstructure was observed in NS-activated system. The additional, soluble silicates in the sodium silicate activator facilitated the formation of more reaction products within the matrix, leading to a compact microstructure. The increased formation of reaction products, primarily N-(C-)A-S-H gel, in the NS-activated system will be further corroborated by thermodynamic modeling results.

As shown in Fig. 5 (b), three phases in the AAFA pastes, i.e. unreacted fly ash, reaction products and pores, were segmented according to the method described in Section 2.2.1. Through this segmentation, it becomes possible to identify not only the fly ash particles with clear edges, but also those small fly ash entities lacking distinct edges after dissolution. This enables us to determine the quantity of fly ash, and thus its reaction degree. The reaction degree at 7 and 28 days obtained via image analysis is listed in Table 2. Both systems show a slight increase in reaction degree from 7 to 28 days. The standard deviation, ranging from 3 to 6%, is within a reasonable range for image analysis, as supported by [71]. The reaction degree at 7 days will be used to calculate Q_{max} in Eq. (2), which will be further discussed in Section 3.2.2.

The chemical compositions, in terms of molar Si/Al and Ca/Al ratios, of the reaction products are further investigated from the elemental mapping results, as shown in Fig. 5 (c) and (d), respectively. For NH-activated system, the Si/Al ratio predominantly remains below 3 in most areas of the reaction product, while the NS-activated system exhibits a Si/Al ratio exceeding 3 across the majority of the reaction product. This arises not only from the formation of the N-(C-)A-S-H gel with a higher Si/Al ratio, but also from the additional Si species brought by sodium silicate activator. Correspondingly, the average Si/Al ratios of the reaction products, as listed in Table 2 (including 7 days and 28 days), also follows the same trend. Furthermore, the NH-activated system displays an upward trend in the Si/Al ratio over time, while the NS-activated system demonstrates a decline in Si/Al ratio over the same period. This suggests that the stability of N-(C-)A-S-H gel with a Si/Al ratio surpassing 3 may be thermodynamically less favorable, as also visible in the higher solubility of N-A-S-H gel with a higher Si/Al ratio ([13], as discussed in more detail in Section 3.3.1). Additionally, for both systems, a molar Ca/Al ratio (see Fig. 5 (d) and Table 2) of around 0.2–0.3 was observed homogeneously distributed within the reaction product zone, which confirms that Ca tends to be incorporated into N-A-S-H gel to form N-(C-)A-S-H gel even in low-Ca alkali-activated binder. This composition also served as guidance to synthesize N-C-A-S-H gels, as discussed later.

3.1.5. Pore solution analysis

The concentrations of Si, Al, Na, K, Fe, Ca, Mg and OH^- in the pore solutions in the AAFA pastes are presented in Fig. 6. A decrease in concentrations is observed from 7 days to 28 days for all elements, indicating that the formation of solid reaction products dominates over the dissolution of fly ash. In addition, the elemental concentrations in NH-activated system are higher than its counterpart. This can be attributed to two main factors. For one thing, NH-activated system has a higher pH, which increases ion solubility, allowing more ions to remain in the pore solution. For another, the soluble silicate in sodium silicate accelerates the formation of reaction products. These combined effects lead to a higher elemental concentration in the pore solution of NH-activated system than its counterpart.

3.2. Reaction kinetics

3.2.1. Isothermal calorimetry

The rate of heat evolution and cumulative heat release of AAFA pastes determined by isothermal calorimetry are shown in Fig. 7. The NH-activated system exhibits multi-peaks calorimetric response, while only a single wide exothermic peak is observed in the NS-activated system. For both systems, the initial dissolution peak is captured completely due to the utilization of in-situ approach. The NH-activated system with a higher pH shows a quicker and stronger calorimetric response than the NS-activated system. After the initial stage of dissolution, the NH-activated system undergoes an induction period, followed by two distinct small peaks, which have been attributed to the polycondensation process [72]. The presence of these individual peaks suggests a multi-step reaction, in alignment with the gel evolution theory [73,74], as previously also found in [52]. In contrast, the NS-activated system experiences polycondensation initially due to the high availability of soluble silica in the activator, which allows the formation of aluminosilicate oligomers after the dissolution of fly ash. As a result, the exothermic responses resulting from dissolution and polycondensation are superimposed, leading to the observation of a single wide peak in the NS-activated system [75].

With the determined cumulative heat $Q(7d)$ and reaction degree at 7 days derived from image analysis, the maximum cumulative heat $Q_{\max}$ can be calculated using Eq. (2). In addition, calorimetric data (Fig. 7 (b)) was fitted with the parameters listed in Table 3, which will be used to calculate the reaction degree over time (see Eq. (4)) in the following section.

3.2.2. Degree of reaction over time

The reaction degree of fly ash obtained from image analysis (Eq. (1)) and calculated based on the fitting calorimetric data (Eq. (4)) are shown in Fig. 8. The reaction degree of fly ash exhibits a notable rise during the initial days and becomes relatively stable afterwards, indicating a slower reaction rate as previously observed in [76]. The reduced reaction rate at later stage can be attributed to the reduced pH value and the increasing formation of reaction products over time, which limits the interaction between fly ash and alkali activator solution. After the initial days, the reaction degree of fly ash in the NH-activated system and NS-activated system are comparable. Sodium hydroxide, owing to its high pH, enhances the dissolution of fly ash at early times, while sodium silicate aids in the formation of reaction products. As a result, the fraction of fly ash that reacted is comparable in these two systems. Despite similar reaction degrees, the microstructure in the NS-activated system is more compact than the NH-activated system due to a higher fraction of reaction products, as shown in Table 2. Overall, the reaction degree of fly ash between 7 and 28 days falls within the range of approximately

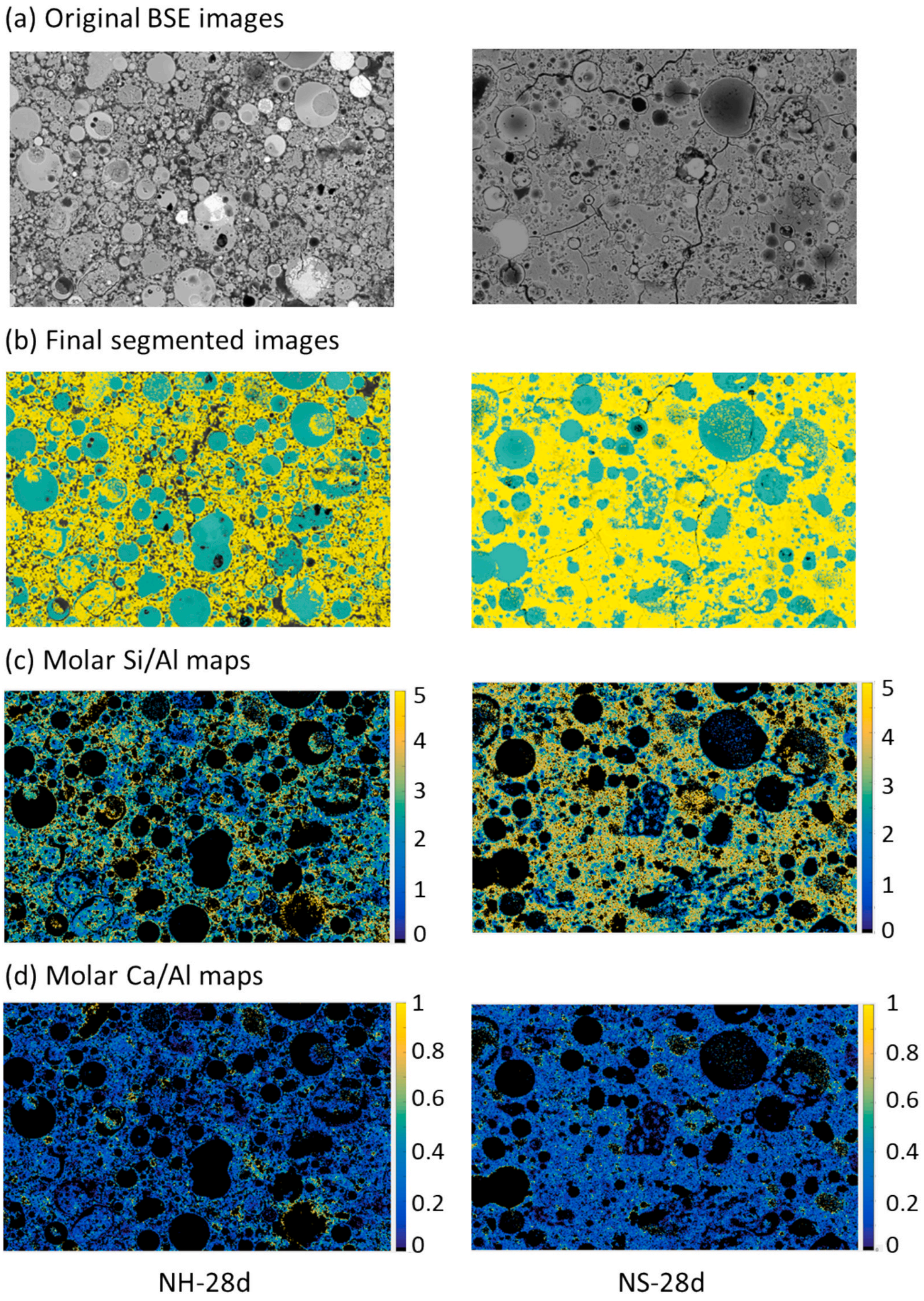

Fig. 5. (a) Original SEM-BSE micrographs of the NH (left) and NS (right) activated fly ash pastes cured at 28 days. (b) Segmented micrographs of AAFA pastes. Green zone: unreacted fly ash; Yellow zone: reaction products; Dark zone: voids. (c) Molar Si/Al maps for the reaction products in AAFA pastes. (d) Molar Ca/Al maps for the reaction products in AAFA pastes. Only samples cured 28 days are shown for clarity, while samples cured at 7 days are provided in Appendix (Fig. A3). (For interpretation of the references to colour in this figure legend, the reader is referred to the web version of this article.)

30–45%, in agreement with the results in [31,76], of which the content of amorphous phase in fly ash and mixture design are similar to this study. These reaction kinetics will be utilized in subsequent thermodynamic modeling. It should be noted that while testing errors in the reaction degree might slightly influence the reaction kinetics, they are not expected to significantly affect the outcomes of the thermodynamic modeling.

3.3. Thermodynamic modeling of AAFA

3.3.1. Thermodynamic dataset of N-(C-)A-S-H gels

Different N-C-A-S-H gels were synthesized (chemical compositions in Table A2 and XRD patterns in Fig. A4) and their solubility determined from undersaturation. The N-C-A-S-H gels with a small amount of Ca have a similar aluminosilicate structure as the N-A-S-H gel, albeit with a less crosslinked framework [77], which is also supported by FTIR result

Table 2
Information obtained via image analysis: average molar Si/Al and Ca/Al ratio in the reaction products, reaction degree of fly ash, volume fraction of reaction products.

Samples	Si/Al	Ca/Al	Reaction degree (%)	Volume fraction of reaction products
NH-7d	2.3 ± 0.9	0.21 ± 0.17	34 ± 6	54%
NH-28d	2.5 ± 0.9	0.21 ± 0.16	39 ± 5	62%
NS-7d	3.2 ± 1.0	0.27 ± 0.18	34 ± 5	61%
NS-28d	3.1 ± 1.0	0.22 ± 0.16	38 ± 3	67%

in this work. Pure N-C-A-S-H gels with a Si/Al ratio of 2–3 and a Ca/Al ratio of 0.25–0.5 were obtained. Based on the dissolution experiments with a duration of 60 days, their solubilities at 25 °C were calculated, as detailed in Tables A3 and A4. Fig. 9 illustrates the effect of Ca/Al ratio on the log K_{sp} of N-(C-)A-S-H gels. Regardless of Si/Al ratio, the presence of Ca in the gel stabilized the gel as visible by the strong decrease of the solubility products (log K_{sp}) with the Ca-content.

Together with the thermodynamic data of N-A-S-H gels determined in [13], a thermodynamic database of N-(C-)A-S-H gels is thus available for thermodynamic modeling of AAFA, as summarized in Table 4.

3.3.2. *Calculated phase assemblages of AAFA paste*

3.3.2.1. Phase assemblages over time. Thermodynamic modeling of AAFA paste, in combination with the kinetic process developed in Fig. 8, is carried out to study the expected evolution of both solid and aqueous phases as a function of time. The calculated evolution of the phase assemblages of AAFA pastes is shown in Fig. 10. Over time, there is an observable decrease in the fraction of fly ash, coinciding mainly with the formation of N-(C-)A-S-H gel in both NH and NS-activated systems.

The NS-activated system yields a greater quantity of N-(C-)A-S-H gel than that in the NH-activated system, in line with the findings of TGA and SEM-EDS mapping. In addition, some secondary reaction products are predicted in both systems, including C-(N-)A-S-H gel, brucite ($Mg(OH)_2$), magnesium silicate hydrates (MSH) and microcrystalline ferrihydrite

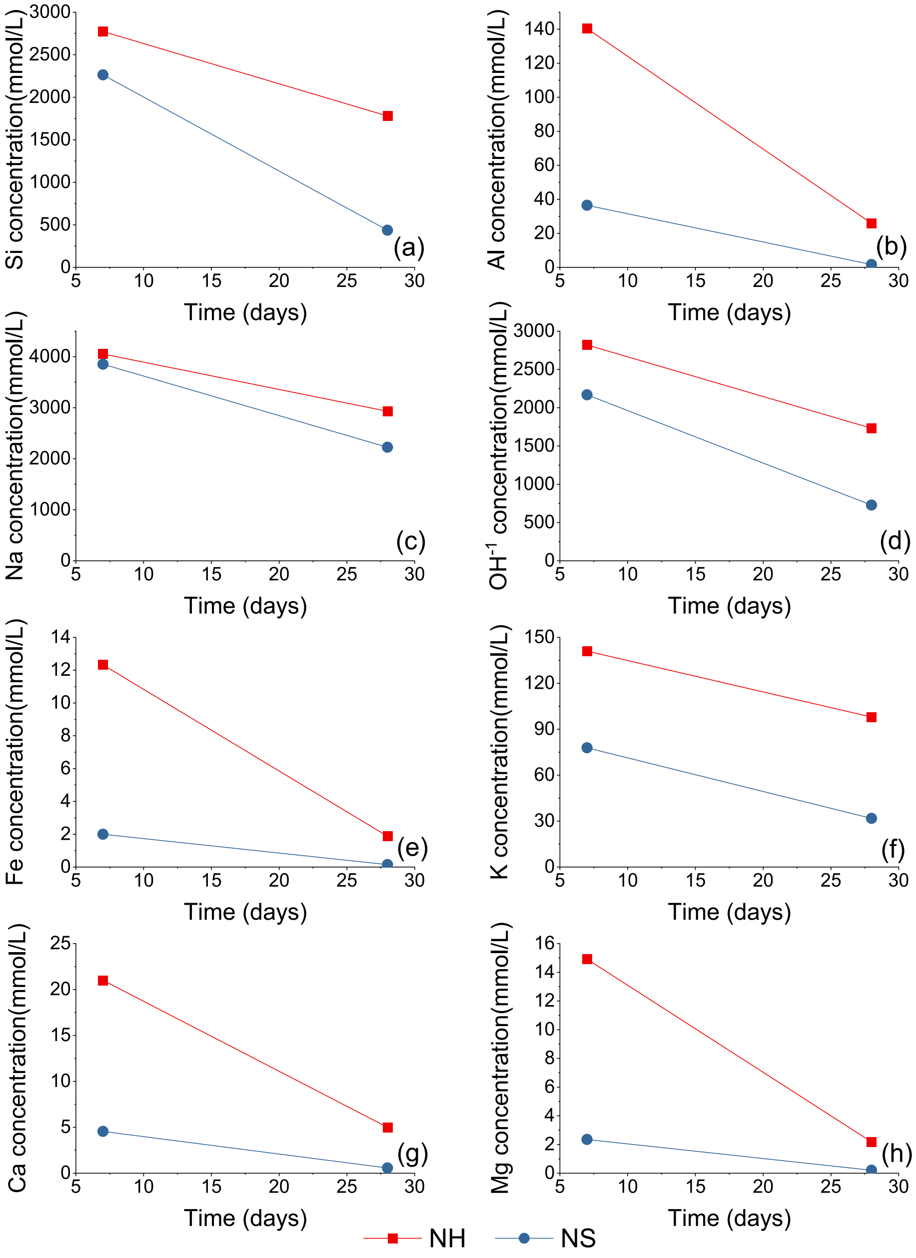

Fig. 6. Elementary concentrations of the pore solutions in AAFA pastes.

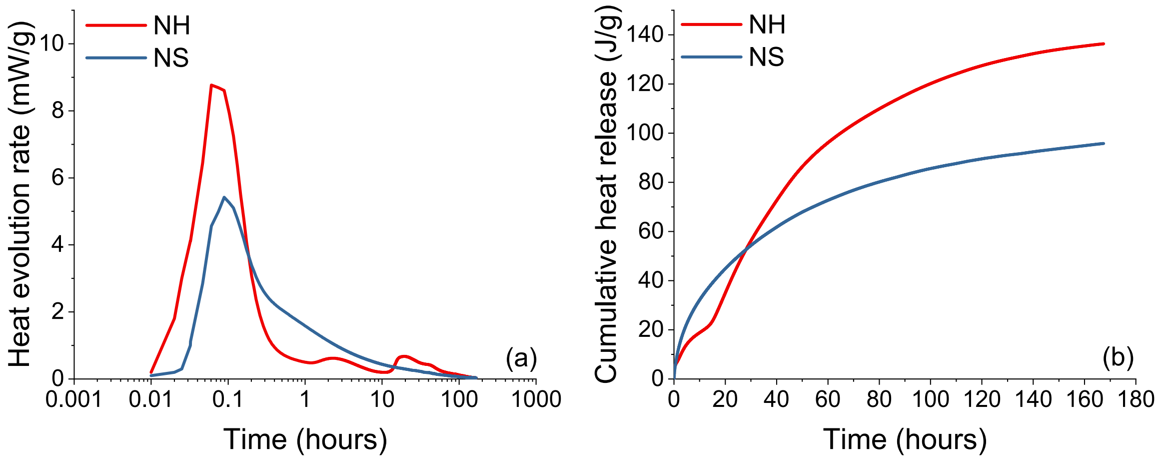

Fig. 7. Heat evolution rate and cumulative heat release for AAFA pastes cured at 40 °C.

Table 3
The parameters in Eqs. (2) and (3).

Sample	Q(7*d*) (J/g)	Q_{max} (J/g)	Q_{max_fit} (J/g)	λ	β
NH	138	400	195	38.6	0.74
NS	97	282	146	26.7	0.46

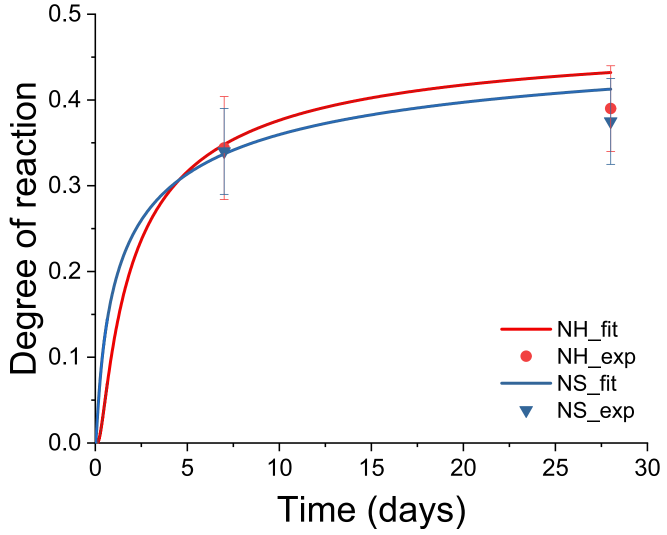

Fig. 8. Degree of reaction of fly ash in AAFA paste as a function of time. NH_fit and NS_fit refer to the degree of reaction calculated via Eq. (4), while NH_exp and NS_exp refer to the degree of reaction obtained from image analysis.

(FeOOH, mc refers to microcrystalline). These secondary phases are challenging to detect by experimental techniques due to their minor quantities. The existence of some C-(N-)A-S-H gel is consistently calculated in the NH-activated system, whereas only a negligible amount of C-(N-)A-S-H gel is expected to form initially (0–2 days) in the NS-activated system. This agrees with the XRD results (see Fig. 2), where a very small peak at around 29° 2θ (corresponding to C-(N-)A-S-H gel) can be found in all NH-activated samples but is absent in all NS-activated samples as well as with the FTIR results in Fig. 3. In addition, the presence of hydroxysodalite (SOD(OH)) in NH-activated system and its absence in NS-activated system is also in accordance with the XRD and FTIR results.

3.3.2.2. Fractions of end members in simulated N-(C-)A-S-H gels. The main reaction product, the N-(C-)A-S-H gel, is expected to vary between the NH- and NS-activated systems. The composition in the N-(C-)A-S-H gel can be calculated based on solid solution model used (see Table 4) as illustrated in Fig. 11. For the NH-activated system, the principal components in N-(C-)A-S-H gel is N-A-S-H gel with a Si/Al ratio of 1 (nash1), followed by N-C-A-S-H gel with a Si/Al ratio of 3 and a Ca/Al ratio of 0.5 (ncash3_0.5). In contrast, the NS-activated system primarily yields ncash3_0.5 as the dominant component, and it also forms a greater abundance of high Si/Al gels (e.g., nash2, ncash3_0.25) while producing fewer low Si/Al gels (specifically nash1) compared to the NH-activated system. This indicates that the N-(C-)A-S-H gel formed in the NS-activated system has a higher Si/Al ratio than that in the NH-activated system, which aligns with the SEM-EDS mapping results (see Table 3). It is interesting to observe the absence of N-A-S-H gel with a Si/Al ratio of 3 (nash3) in both systems, even though high Si/Al N-(C-)A-S-H gel is expected to form in NS-activated system. The reason behind it would be the high solubility of nash3 [13].

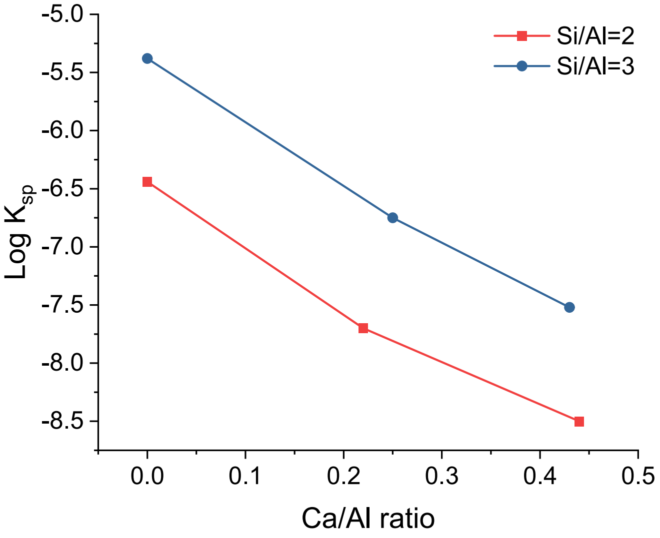

Fig. 9. Log K_{sp} of N-(C-)A-S-H gels at 25 °C as a function of Ca/Al.

3.3.2.3. Si/Al and Ca/Al ratios in the reaction products. Fig. 12 provides an overview of the Si/Al and Ca/Al ratios in the solid reaction products, both from experimental data and thermodynamic modeling. The simulated Si/Al ratio in the NH-activated fly ash cured from 7 to 28 days ranges from 1.6 to 1.7, which is slightly smaller than that in SEM-EDS mapping results (from 2.3 to 2.5). As expected, a higher simulated Si/Al ratio in the NS-activated system is observed compared to its counterpart. However, the discrepancy between experimental data and thermodynamic modeling data is more pronounced in the NS-activated

Table 4
Standard thermodynamic properties of N-(C-)A-S-H gels at 25 °C.

Samples	N-(C-)A-S-H gels	$\Delta_f G^0$ (kJ/mol)	$\Delta_f H^0$ (kJ/mol)	S^0 (J/mol/K)	C_p^0 (J/mol/K)
nash1[a]	$Na_{0.92}Al_{0.92}Si_1O_{3.84}\cdot 0.54H_2O$	−2012.05	−2157.26	125	153
nash2[a]	$Na_{0.5}Al_{0.5}Si_1O_3\cdot 0.35H_2O$	−1497.86	−1601.24	101	106
nash3[a]	$Na_{0.36}Al_{0.36}Si_1O_{2.72}\cdot 0.31H_2O$	−1299.11	−1425.58	73	92
ncash2_0.25	$Na_{0.5}Ca_{0.11}Al_{0.5}Si_1O_{3.11}\cdot 0.46H_2O$	−1601.60	−1719.89	93	116
ncash2_0.5	$Na_{0.46}Ca_{0.2}Al_{0.46}Si_1O_{3.12}\cdot 0.47H_2O$	−1621.68	−1740.18	96	117
ncash3_0.25	$Na_{0.46}Ca_{0.08}Al_{0.32}Si_1O_{2.79}\cdot 0.41H_2O$	−1411.41	−1513.32	95	105
ncash3_0.5	$Na_{0.48}Ca_{0.15}Al_{0.36}Si_1O_{2.93}\cdot 0.48H_2O$	−1514.08	−1625.24	100	113

[a] Data adapted for water content from [13]. Note that the stoichiometry of the water in the formula of N-A-S-H gels is changed slightly compared to [13]. As a result, the thermodynamic data is changed accordingly.

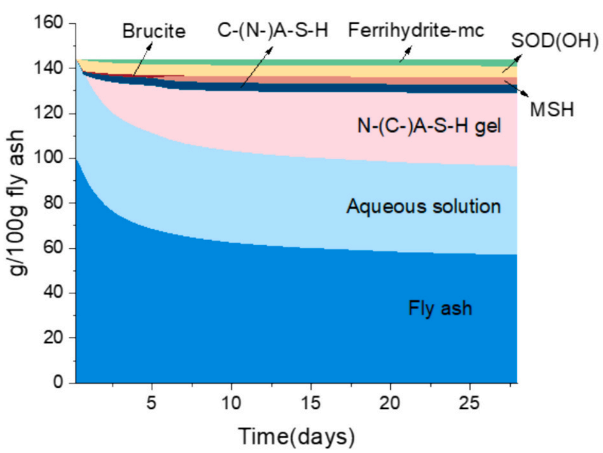

(a) NH

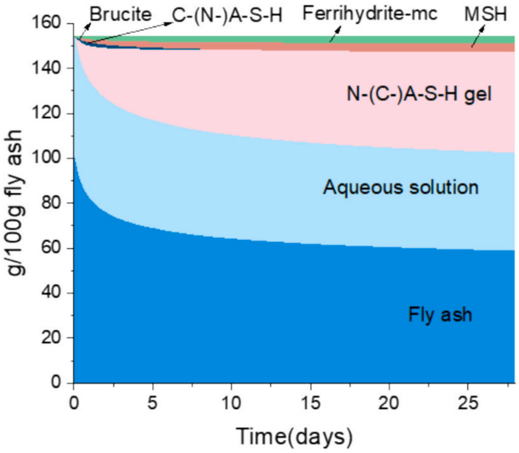

(b) NS

Fig. 10. Simulated phase assemblages of AAFA pastes cured at 40 °C as a function of time. (a) sodium hydroxide activated system, (b) sodium silicate activated system.

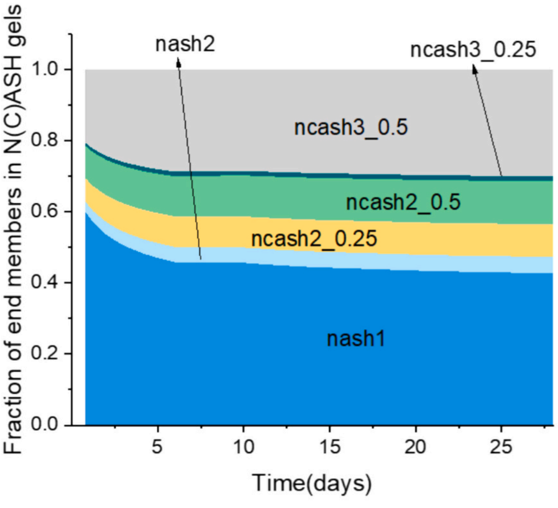

(a) NH-40°C

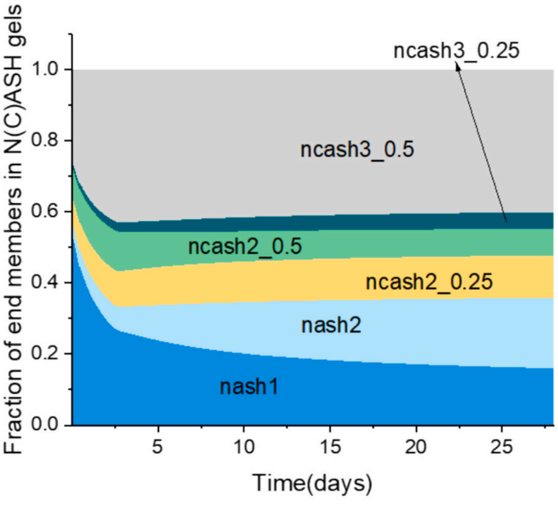

(b) NS-40°C

Fig. 11. Mole proportions of end members in simulated N-(C-)A-S-H gels formed in AAFA pastes cured at 40 °C. (a) sodium hydroxide activated system, (b) sodium silicate activated system. Note that the first number after nash or ncash refers to Si/Al ratio, and the second number after ncash refers to Ca/Al ratio.

system. In this system, the simulated Si/Al ratio ranges from 2.1 to 2.2 in curing age of 7 to 28 days, lower than the SEM-EDS mapping results (from 3.2 to 3.0). The reasons for the underestimation of simulated Si/Al ratio in solid reaction products include two parts. Firstly, in the thermodynamic modeling, lower Si/Al N-(C-)A-S-H gel tends to form due to its lower solubility, which has been discussed in [13]. However, in reality, the formation of reaction products is influenced by precipitation kinetics and various other factors beyond solubility, allowing for the potential formation of high Si/Al N-(C-)A-S-H gel, even if it is less thermodynamically favoured. Secondly, the limitation of the N-(C-)A-S-H gel database prevents the formation of N-(C-)A-S-H gel with exceptionally high Si/Al ratios, since the maximum Si/Al ratio in the N-(C-)A-S-H gel database is only up to 3. Consequently, the modeled Si/Al ratio remains below 3, resulting in values lower than those observed in SEM-EDS mapping. In future work, expanding the database to include N-(C-)A-S-H gel with higher Si/Al ratios should be considered. For the Ca/Al

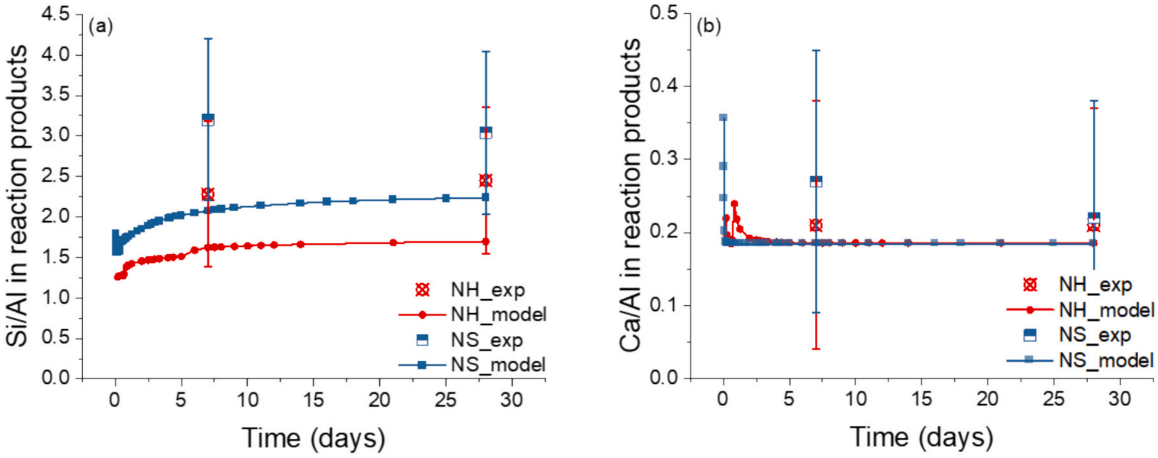

Fig. 12. Experimental and modeling (a) Si/Al ratio and (b) Ca/Al ratio in all reaction products in AAFA pastes cured at 40 °C.

ratio, it can be seen from Fig. 12 (b) that the simulated results in both systems match well with or are slightly smaller than the experimentally measured data.

3.3.2.4. Bound water in the modeled reaction products. The amount of bound water in the modeled reaction products was compared to that obtained from TGA data, as shown in Fig. 13. The modeling result is roughly 10–25% lower than TGA results for both NH- and NS-activated systems. This difference can result from the rough estimation of the fraction of water in the reaction products, as detailed in the methodology (see Section 2.3.2). Additionally, the modeling and the experiments show a similar increase of bound water from 7 days to 28 days. Overall, the bound water calculated from thermodynamic modeling is in good agreement with the experimental data, indicating the accuracy of thermodynamic modeling.

3.3.3. Evolution of compositions in aqueous phases

Fig. 14 presents a comparison between the simulated and experimental elemental concentrations in the pore solution of AAFA pastes. For both NH- and NS-activated systems, both the modeling concentrations of the Si and Al exhibit an increasing trend with time, followed by a subsequent decrease, eventually reaching a stable state, as shown in Fig. 14 (a) and (b). This trend describes well the dissolution of fly ash and the formation of solid reaction products during reactions. Notably, the simulated results closely match the experimental data for the NH-activated system. However, in the NS-activated system, the simulated Si concentration is overestimated, whereas the simulated Al concentration is underestimated at 7 days. These discrepancies can be partly attributed to the underestimation of the Si/Al ratio within the reaction products. More specifically, the rapid decrease in Al concentration in the NS-activated system may result from the overestimation of nash1 formation. As can be seen in Fig. 11 (b), thermodynamic modeling predicts a significant fraction of nash1 forming at an early age in the NS-activated system, which is not expected in reality. The extensive formation of nash1 consumed the majority of available Al, leading to the underestimation of Al. The shortage of Al then limits the further formation of N-(C-)A-S-H gel, resulting in the overestimation of Si. Additionally, the high ionic strength in the NS-activated system, reaching around 10 molarity, challenges the accuracy of the extended Debye-Huckel equation used for computing activity coefficients, designed for an optimal range of 1–2 molarity. As a result, the modeling struggles to accurately depict the chemical environment in the aqueous phase. The Pitzer model, suitable for ~6 molarity, could be one option to improve it. Although the Pitzer model was not used in this work due to its unavailability in GEMS, it is worth investigating it in future work.

For Fig. 14 (c) and (d), a declining trend can be observed both for the concentrations of the Na and OH^- as a function of time in both NH- and NS-activated systems, which is attributed to the consumption of activator. The simulated concentrations of Na and OH^- match well with the experimental results both at 7 days and 28 days for NH-activated system. For NS-activated system, the simulated Na concentration aligns with the experimental data, while the OH^- concentration is underestimated probably affected by the overestimated Si and underestimated Al. Restricting the formation of nash1 could be one of the solutions to improve it.

The simulated concentration of K, as shown in Fig. 14 (e), is higher than experimental data, due to the absence of a solid K-containing Na-K-A-S-H phase in the modeling due to the lack of thermodynamic data. Conversely, an underestimation of the simulated concentration of Fe, Ca and Mg at 7 days can be found in Fig. 14 (f), (g) and (h), respectively. This could be attributed to the overestimation of the amount of different solid phases formed during reaction, since thermodynamic modeling predicts equilibrium condition, while in reality solutions might be oversaturated due to a slow formation of solid phases [18]. Similar findings have been observed in [19,78,79]. In addition, in many cases initially poorly crystalline phases may form, which exhibits higher solubility, leading to higher concentrations in the experiment.

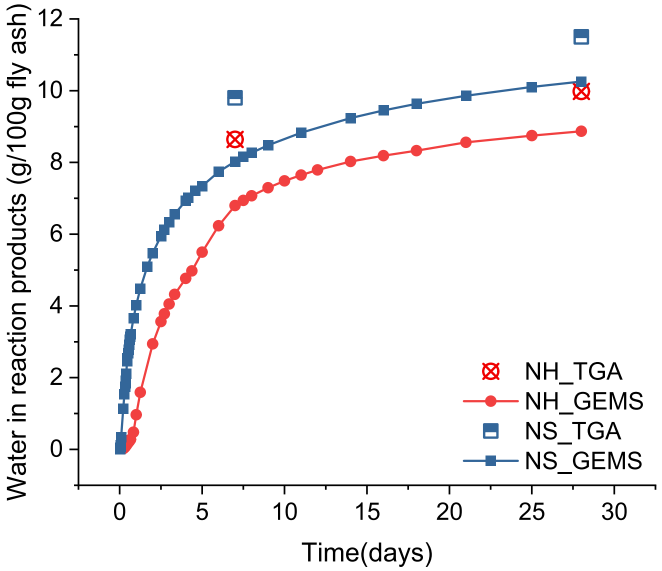

Fig. 13. The amounts of bound water in the modeled reaction products in comparison with TGA data.

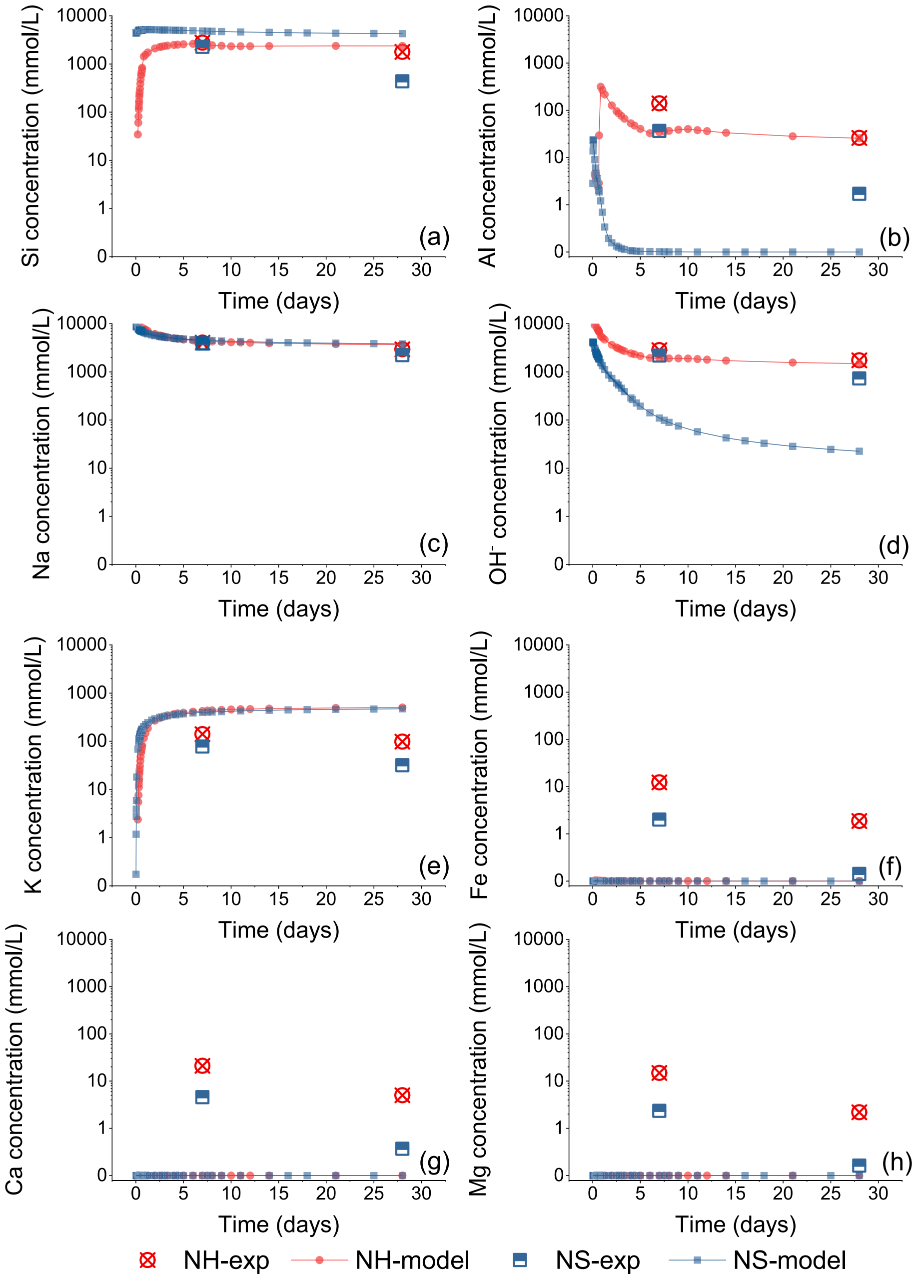

Fig. 14. Experimental and modeling element concentrations in the pore solutions of AAFA pastes cured at 40 °C.

4. Conclusion

In this study, the reaction kinetics and the microstructure of AAFA paste were investigated experimentally. With a newly developed dataset of N-(C-)A-S-H gel, thermodynamic modeling was conducted to study the reactions and phase assemblages of AAFA as a function of time. The results derived from the experiment and modeling were compared. Based on the results and discussion, the following remarks are made:

1. An image analysis method was developed to segment fly ash from AAFA paste based on the elemental composition and grey level, which allows us to determine the reaction degree of fly ash in AAFA.
2. Thermodynamic modeling predicts the experimentally observed phase assemblage in AAFA paste, capturing even minor phases below the experimental detection limits. Both modeling and experimental results indicate that the sodium silicate-activated system forms more reaction products compared to the sodium hydroxide-activated system, resulting also in more bound water in the solid phase.
3. N-(C-)A-S-H gel with a higher Si/Al ratio is formed in the sodium silicate-activated system compared to sodium hydroxide-activated system, again both in the modeling and the experimental findings. However, the simulated Si/Al ratio in the reaction products is lower than the experimentally measured data, especially in the sodium silicate-activated system, while the Ca/Al ratio showed a good agreement between modeling and experimental results.
4. The trends in aqueous Si, Al, Na, and OH^- concentrations closely matched the experimental data for sodium hydroxide-activated fly ash. However, in the sodium silicate-activated fly ash, there was an overestimation of Si concentration and an underestimation of Al concentration. This discrepancy may be attributed to the high ionic strength in the sodium silicate-activated system, the overestimation of the quantity of aqueous silica complexes, or the limited thermodynamic data for N-(C-)A-S-H gel.

This study advances the understanding of AAFA systems by integrating experimental investigation with thermodynamic modeling. The findings in this work highlight the capability of thermodynamic modeling to complement experimental techniques. Moreover, the application of thermodynamic modeling to AAFA can assist in tailoring the mix design of AAFA with the desired properties.

CRediT authorship contribution statement

Yun Chen: Writing – original draft, Methodology, Investigation, Conceptualization. **Bin Ma:** Writing – review & editing, Methodology. **Jiayi Chen:** Methodology. **Zhenming Li:** Writing – review & editing. **Xuhui Liang:** Investigation. **Luiz Miranda de Lima:** Investigation. **Chen Liu:** Writing – review & editing, Investigation. **Suhong Yin:** Supervision. **Qijun Yu:** Supervision. **Barbara Lothenbach:** Writing – review & editing, Methodology. **Guang Ye:** Writing – review & editing, Supervision.

Declaration of competing interest

The authors declare that they have no conflicts of interest.

Acknowledgments

The first author would like to acknowledge China Scholarship Council (Grant No. 201906150022) for the financial support of Yun Chen. Z. Li would like to acknowledge Guangdong Provincial Key Laboratory of Intelligent and Resilient Structures for Civil Engineering (2023B1212010004).

Appendix A

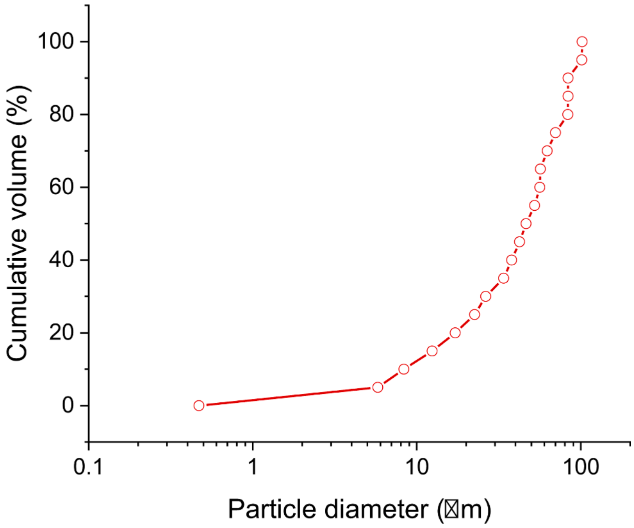

Fig. A1. Particle size distribution of fly ash.

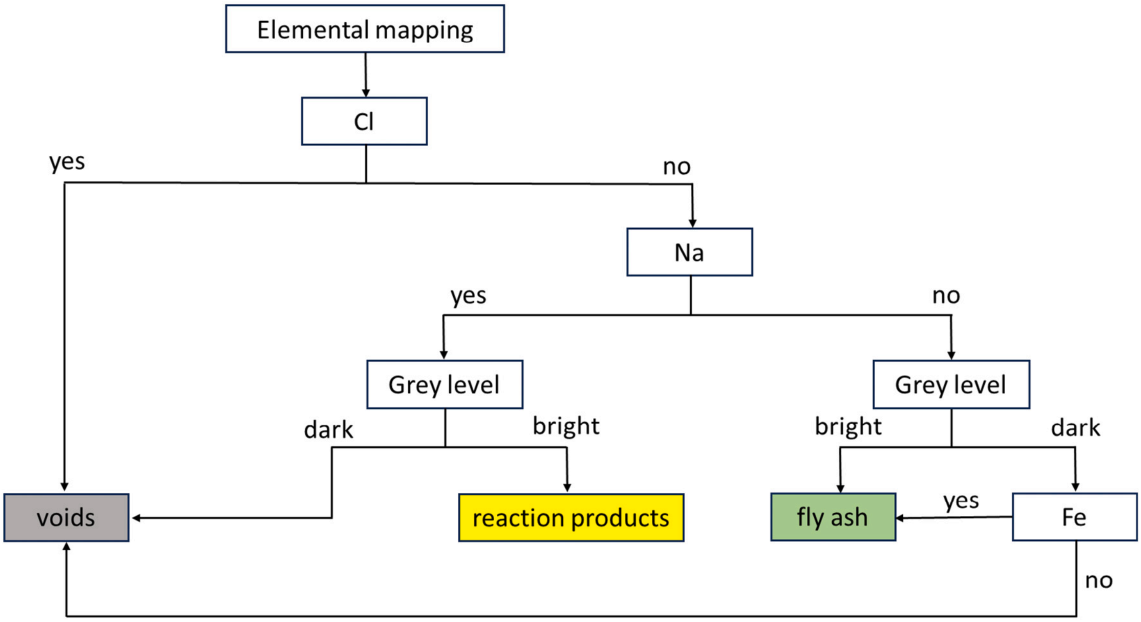

Fig. A2. The overall flowchart of the segmentation of BSE image.

(a) Original BSE images

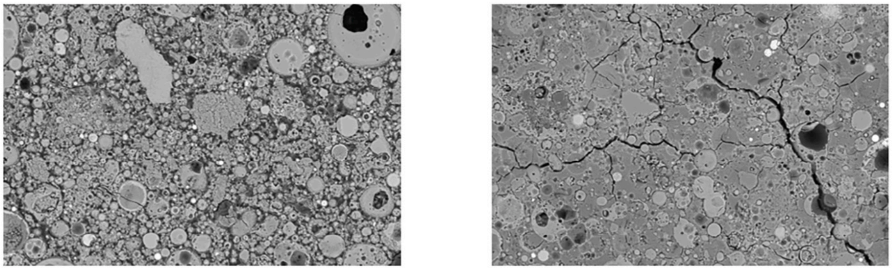

(b) Final segmented images

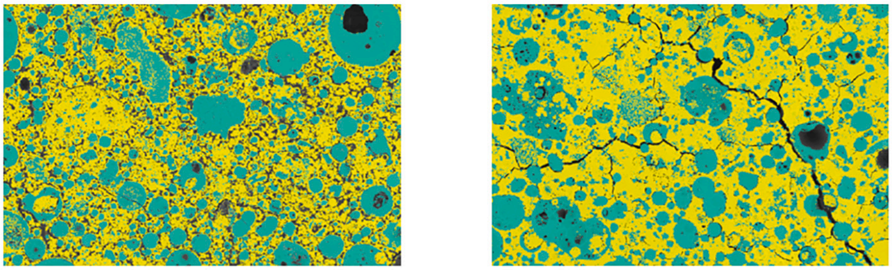

(c) Molar Si/Al maps

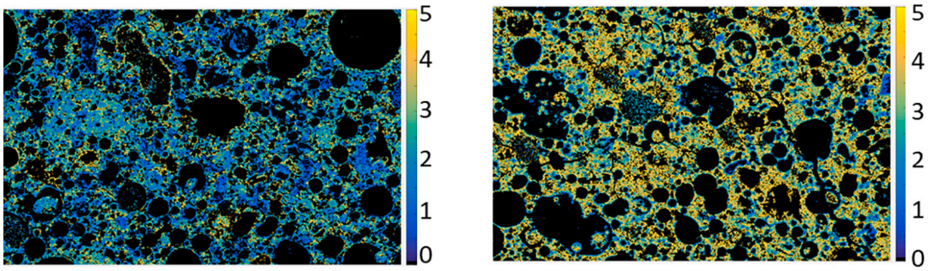

(d) Molar Ca/Al maps

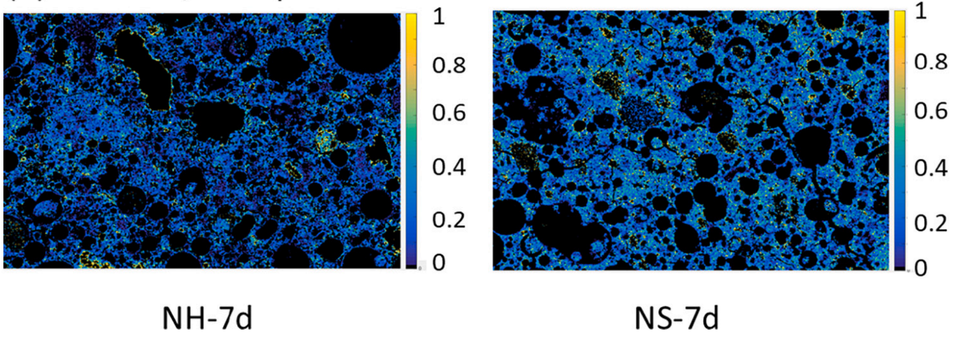

Fig. A3. (a) Original SEM-BSE micrographs of the NH (left) and NS (right) activated fly ash pastes cured at 7 days. (b) Segmented micrographs of AAFA pastes. Green zone: unreacted fly ash; Yellow zone: reaction products; Dark zone: voids. (c) Molar Si/Al maps for the reaction products in AAFA pastes. (d) Molar Ca/Al maps for the reaction products in AAFA pastes. (For interpretation of the references to colour in this figure legend, the reader is referred to the web version of this article.)

Synthesis of N-C-A-S-H gel

For the synthesis of N-C-A-S-H gel with various Si/Al and Ca/Al ratios, a 1 M sodium silicate solution was first mixed with a 0.5 M calcium nitrate solution and the pH regulator, followed by stirring for 30 min following the procedure outlined in [13]. Next, a 1 M aluminum nitrate solution was added slowly to the stirring solution. The quantity of the solutions was adjusted to obtain target Si/Al and Ca/Al ratios, as shown in Table A1. The procedure for the synthesis of N-C-A-S-H gel was carried out for a duration of 1 day at 20 °C. After that, the gel was centrifuged at 5000 rpm for 5 mins and triple-washed by water before drying.

Table A1
Synthesis mixtures for N-C-A-S-H gel.

Samples	Na_2SiO_3	$Al(NO_3)_3$	$Ca(NO_3)_2$	pH regulator	Target Si/Al	Target Ca/Al	pH
NC2_0.25	140 mL	40 mL	24 mL	10 mL NaOH (1 M)	2	0.25	13.55
NC2_0.5	140 mL	40 mL	44 mL	20 mL NaOH (1 M)	2	0.5	13.42
NC3_0.25	240 mL	40 mL	26 mL	10.5 mL HNO_3 (>65%)	3	0.25	13.37
NC3_0.5	240 mL	40 mL	42 mL	8 mL HNO_3 (>65%)	3	0.5	13.54

Note: 'NC' stands for N-C-A-S-H gel; the number after 'NC' refers to the target Si/Al and Ca/Al, respectively.

Chemical compositions and XRD patterns of N-C-A-S-H gels

The XRD pattern shows a single hump at around 30° 2θ for all samples, indicating the formation of pure amorphous N-C-A-S-H gels.

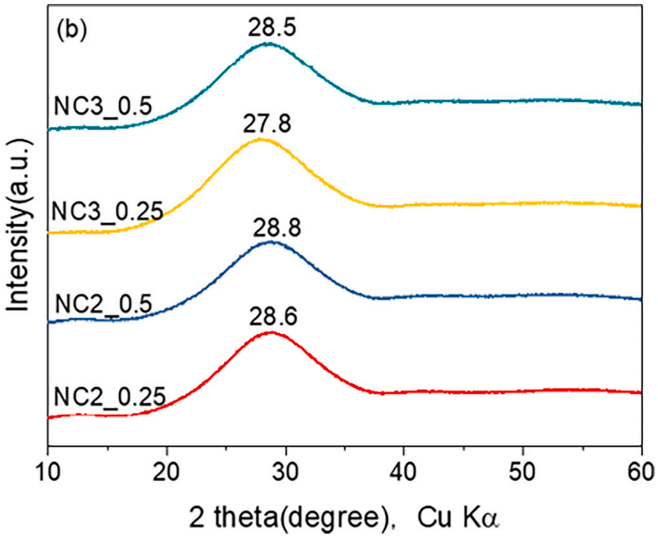

Fig. A4. XRD patterns of the synthesized N-C-A-S-H gels.

As shown in Fig. A5, TGA measurement was performed to determine the amount of non-evaporable water in the synthesized N-C-A-S-H gels. Coupled with the XRF results, the chemical composition of all synthesized N-C-A-S-H gels can be determined, as presented in Table A2.

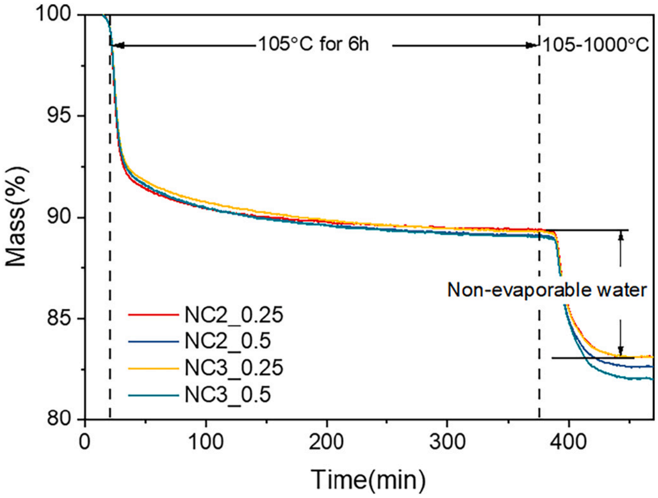

Fig. A5. Thermogravimetric analysis of synthesized N-C-A-S-H gels.

Table A2
Chemical composition of synthesized N-C-A-S-H gels.

Samples	Non-evaporable water	Si/Al	Ca/Al	Chemical composition
NC2_0.25	6.22%	2.04	0.22	$(Na_2O)_{0.25}(CaO)_{0.11}(Al_2O_3)_{0.25}(SiO_2)_1(H_2O)_{0.47}$
NC2_0.5	6.16%	2.20	0.44	$(Na_2O)_{0.23}(CaO)_{0.2}(Al_2O_3)_{0.23}(SiO_2)_1(H_2O)_{0.42}$
NC3_0.25	6.84%	3.10	0.25	$(Na_2O)_{0.23}(CaO)_{0.08}(Al_2O_3)_{0.16}(SiO_2)_1(H_2O)_{0.44}$
NC3_0.5	6.08%	2.83	0.43	$(Na_2O)_{0.24}(CaO)_{0.15}(Al_2O_3)_{0.18}(SiO_2)_1(H_2O)_{0.42}$

Solubility products of N-C-A-S-H gels

Table A3
Average elemental concentrations (mmol/L) and pH in the filtrated solution of the solubility test after an equilibration time of 60 days.

Samples	Ca	Na	Si	Al	pH
NC2_0.25	0.08	17.28	9.34	0.32	11.71
NC2_0.5	0.09	22.07	12.01	0.18	11.86
NC3_0.25	0.08	20.76	16.98	0.15	11.49
NC3_0.5	0.20	21.24	16.89	0.33	11.52

The solubility products of N-(C-)A-S-H gels at 25 °C were calculated based on the dissolution reactions listed in Table A4 and using the measured composition of the gels as given in Table A2.

Table A4
The log solubility products of N-(C-)A-S-H gels per 1 mol of Si at 25 °C.

N-C-A-S-H gels	Dissolution reactions	Log K_{sp}
N1	$(Na_2O)_{0.46}(Al_2O_3)_{0.46}(SiO_2)_1(H_2O)_{0.54} \rightarrow 0.92\ Na^+ + 0.92\ AlO_2^- + SiO_2^0 + 0.54\ H_2O$	−8.47
N2	$(Na_2O)_{0.25}(Al_2O_3)_{0.25}(SiO_2)_1(H_2O)_{0.35} \rightarrow 0.5\ Na^+ + 0.5\ AlO_2^- + SiO_2^0 + 0.35\ H_2O$	−6.44
N3	$(Na_2O)_{0.18}(Al_2O_3)_{0.18}(SiO_2)_1(H_2O)_{0.31} \rightarrow 0.36\ Na^+ + 0.36\ AlO_2^- + SiO_2^0 + 0.31\ H_2O$	−5.38
NC2_0.25	$(Na_2O)_{0.25}(CaO)_{0.11}(Al_2O_3)_{0.25}(SiO_2)_1(H_2O)_{0.47} \rightarrow 0.11Ca^{2+} + 0.5Na^+ + 0.5AlO_2^- + SiO_2^0 + 0.22OH^- + 0.36H_2O$	−7.70
NC2_0.5	$(Na_2O)_{0.23}(CaO)_{0.2}(Al_2O_3)_{0.23}(SiO_2)_1(H_2O)_{0.42} \rightarrow 0.2Ca^{2+} + 0.46Na^+ + 0.46AlO_2^- + SiO_2^0 + 0.4OH^- + 0.22H_2O$	−8.50
NC3_0.25	$(Na_2O)_{0.23}(CaO)_{0.08}(Al_2O_3)_{0.16}(SiO_2)_1(H_2O)_{0.44} \rightarrow 0.08Ca^{2+} + 0.46Na^+ + 0.32AlO_2^- + SiO_2^0 + 0.3OH^- + 0.29H_2O$	−6.75
NC3_0.5	$(Na_2O)_{0.24}(CaO)_{0.15}(Al_2O_3)_{0.18}(SiO_2)_1(H_2O)_{0.42} \rightarrow 0.15Ca^{2+} + 0.48Na^+ + 0.36AlO_2^- + SiO_2^0 + 0.42OH^- + 0.21H_2O$	−7.52

Data availability

Data will be made available on request.

References

[1] G. Kovalchuk, A. Fernández-Jiménez, A. Palomo, Alkali-activated fly ash: effect of thermal curing conditions on mechanical and microstructural development - part II, Fuel 86 (2007) 315–322, https://doi.org/10.1016/j.fuel.2006.07.010.

[2] Y. Ding, J.G. Dai, C.J. Shi, Mechanical properties of alkali-activated concrete: a state-of-the-art review, Constr. Build. Mater. 127 (2016) 68–79, https://doi.org/10.1016/j.conbuildmat.2016.09.121.

[3] K. Arbi, M. Nedeljković, Y. Zuo, G. Ye, A review on the durability of alkali-activated fly ash/slag systems: advances, issues, and perspectives, Ind. Eng. Chem. Res. 55 (2016) 5439–5453, https://doi.org/10.1021/acs.iecr.6b00559.

[4] J. Zhang, C. Shi, Z. Zhang, Z. Ou, Durability of alkali-activated materials in aggressive environments: a review on recent studies, Constr. Build. Mater. 152 (2017) 598–613, https://doi.org/10.1016/j.conbuildmat.2017.07.027.

[5] A. Fernández-Jiménez, A. Palomo, C. López-Hombrados, Engineering properties of compacted fly ash, ACI Mater. J. 3 (2006) 106–112, https://doi.org/10.1061/jsfeaq.0001744.

[6] A. Fernández-Jiménez, A. Palomo, New cementitious materials based on alkali-activated fly ash: performance at high temperatures, J. Am. Ceram. Soc. 91 (2008) 3308–3314.

[7] M.T. Junaid, A. Khennane, O. Kayali, A. Sadaoui, D. Picard, M. Fafard, Aspects of the deformational behaviour of alkali activated fly ash concrete at elevated temperatures, Cem. Concr. Res. 60 (2014) 24–29, https://doi.org/10.1016/j.cemconres.2014.01.026.

[8] B. Lothenbach, D.A. Kulik, T. Matschei, M. Balonis, L. Baquerizo, B.Z. Dilnesa, G. D. Miron, R. M., Cemdata18: a chemical thermodynamic database for hydrated Portland cements and alkali-activated materials, Cem. Concr. Res. (2019) 472–506, https://doi.org/10.1109/ICCPS.2014.6843714.

[9] B. Lothenbach, M. Zajac, Application of thermodynamic modelling to hydrated cements, Cem. Concr. Res. 123 (2019) 105779, https://doi.org/10.1016/j.cemconres.2019.105779.

[10] R.J. Myers, B. Lothenbach, S.A. Bernal, J.L. Provis, Thermodynamic modelling of alkali-activated slag cements, Appl. Geochem. 61 (2015) 233–247, https://doi.org/10.1016/j.apgeochem.2015.06.006.

[11] X. Ke, Y. Duan, Coupling machine learning with thermodynamic modelling to develop a composition-property model for alkali-activated materials, Compos. Part B Eng. 216 (2021) 108801, https://doi.org/10.1016/j.compositesb.2021.108801.

[12] R. Caron, R.A. Patel, G.D. Miron, C. Le Galliard, B. Lothenbach, F. Dehn, Microstructure development of slag activated with sodium silicate solution: experimental characterization and thermodynamic modeling, J. Build. Eng. 71 (2023) 106398, https://doi.org/10.1016/j.jobe.2023.106398.

[13] Y. Chen, L.M. de Lima, Z. Li, B. Ma, B. Lothenbach, Synthesis, solubility and thermodynamic properties of N-A-S-H gels with various target Si/Al ratios, Cem. Concr. Res. 180 (2024) 107484, https://doi.org/10.1016/j.cemconres.2024.107484.

[14] I. García-Lodeiro, A. Fernández-Jiménez, A. Palomo, Variation in hybrid cements over time. Alkaline activation of fly ash-portland cement blends, Cem. Concr. Res. 52 (2013) 112–122, https://doi.org/10.1016/j.cemconres.2013.03.022.

[15] Z. Zhang, L. Li, X. Ma, H. Wang, Compositional, microstructural and mechanical properties of ambient condition cured alkali-activated cement, Constr. Build. Mater. 113 (2016) 237–245, https://doi.org/10.1016/j.conbuildmat.2016.03.043.

[16] I. Ismail, S.A. Bernal, J.L. Provis, R. San Nicolas, S. Hamdan, J.S.J. Van Deventer, Modification of phase evolution in alkali-activated blast furnace slag by the incorporation of fly ash, Cem. Concr. Compos. 45 (2014) 125–135, https://doi.org/10.1016/j.cemconcomp.2013.09.006.

[17] N.K. Lee, H.K. Lee, Reactivity and reaction products of alkali-activated, fly ash/slag paste, Constr. Build. Mater. 81 (2015) 303–312, https://doi.org/10.1016/j.conbuildmat.2015.02.022.

[18] B. Lothenbach, Thermodynamic equilibrium calculations in cementitious systems, Mater. Struct. 43 (2010) 1413–1433, https://doi.org/10.1617/s11527-010-9592-x.

[19] Y. Zuo, M. Nedeljković, G. Ye, Coupled thermodynamic modelling and experimental study of sodium hydroxide activated slag, Constr. Build. Mater. 188 (2018) 262–279, https://doi.org/10.1016/j.conbuildmat.2018.08.087.

[20] A. Fernández-Jiménez, A.G. de la Torre, A. Palomo, G. López-Olmo, M.M. Alonso, M.A.G. Aranda, Quantitative determination of phases in the alkaline activation of fly ash. Part II: degree of reaction, Fuel 85 (2006) 1960–1969, https://doi.org/10.1016/j.fuel.2006.04.006.

[21] X. Gao, Q.L. Yu, H.J.H. Brouwers, Apply 29Si, 27Al MAS NMR and selective dissolution in identifying the reaction degree of alkali activated slag-fly ash composites, Ceram. Int. 43 (2017) 12408–12419, https://doi.org/10.1016/j.ceramint.2017.06.108.

[22] L. Li, J. Yang, H. Li, Quantifying the microstructure and phase assemblage of alkali-activated fly ash/slag materials by EDS mapping analysis, Mater. Des. 234 (2023) 112320, https://doi.org/10.1016/j.matdes.2023.112320.

[23] M. Ben Haha, K. De Weerdt, B. Lothenbach, Quantification of the degree of reaction of fly ash, Cem. Concr. Res. 40 (2010) 1620–1629, https://doi.org/10.1016/j.cemconres.2010.07.004.

[24] ASTM C618-19, Standard Specification for Coal Fly Ash and Raw or Calcined Natural Pozzolan for Use in Concrete, ASTM International, West Conshohocken, 2019.

[25] R. Snellings, J. Chwast, Ö. Cizer, N. De Belie, Y. Dhandapani, P. Durdzinski, J. Elsen, J. Haufe, D. Hooton, C. Patapy, M. Santhanam, K. Scrivener, D. Snoeck, L. Steger, S. Tongbo, A. Vollpracht, F. Winnefeld, B. Lothenbach, RILEM TC-238 SCM recommendation on hydration stoppage by solvent exchange for the study of hydrate assemblages, Mater. Struct. Constr. 51 (2018), https://doi.org/10.1617/s11527-018-1298-5.

[26] N. Doebelin, R. Kleeberg, Profex: a graphical user interface for the Rietveld refinement program BGMN, J. Appl. Crystallogr. 48 (2015) 1573–1580.

[27] K. Scrivener, R. Snellings, B. Lothenbach, A Practical Guide to Microstructural Analysis of Cementitious Materials, 2018, https://doi.org/10.1201/b19074.

[28] T. Wang, T. Ishida, R. Gu, A study of the influence of crystal component on the reactivity of low-calcium fly ash in alkaline conditions based on SEM-EDS, Constr. Build. Mater. 243 (2020) 118227, https://doi.org/10.1016/j.conbuildmat.2020.118227.

[29] W. Wilson, L. Sorelli, A. Tagnit-Hamou, Automated coupling of NanoIndentation and Quantitative Energy-Dispersive Spectroscopy (NI-QEDS): a comprehensive method to disclose the micro-chemo-mechanical properties of cement pastes, Cem. Concr. Res. 103 (2018) 49–65, https://doi.org/10.1016/j.cemconres.2017.08.016.

[30] J.E. Rossen, K.L. Scrivener, Optimization of SEM-EDS to determine the C–A–S–H composition in matured cement paste samples, Mater. Charact. 123 (2017) 294–306, https://doi.org/10.1016/j.matchar.2016.11.041.

[31] Y. Ma, Microstructure and Engineering Properties of Alkali Activated Fly Ash - As an Environment Friendly Alternative to Portland Cement, 2013, https://doi.org/10.4233/uuid:dc26be48-b007-4c17-973f-e386e4dcf821.

[32] N. Otsu, A threshold selection method from gray-level histograms, IEEE Trans. Syst. Man Cybern. 9 (1979) 62–66, https://doi.org/10.1109/TSMC.1979.4310076.

[33] J. Kempl, O. Çopuroğlu, EH-pH- and main element analyses of Blast Furnace Slag Cement paste pore solutions activated with sodium monofluorophosphate - implications for carbonation and self-healing, Cem. Concr. Compos. 71 (2016) 63–76, https://doi.org/10.1016/j.cemconcomp.2016.05.004.

[34] J. Duchesne, M.A. Bérubé, Evaluation of the validity of the pore solution expression method from hardened cement pastes and mortars, Cem. Concr. Res. 24 (1994) 456–462, https://doi.org/10.1016/0008-8846(94)90132-5.

[35] F. Chayes, Petrographic Modal Analysis: An Elementary Statistical Appraisal (No Title), 1956.

[36] G. Fang, Q. Wang, M. Zhang, In-situ X-ray tomographic imaging of microstructure evolution of fly ash and slag particles in alkali-activated fly ash-slag paste, Compos. Part B Eng. 224 (2021) 109221, https://doi.org/10.1016/j.compositesb.2021.109221.

[37] Y. Zuo, Experimental Study and Numerical Simulation of the Reaction Process and Microstructure Formation of Alkali-activated Materials, 2019, https://doi.org/10.4233/uuid.

[38] D. Ravikumar, N. Neithalath, Reaction kinetics in sodium silicate powder and liquid activated slag binders evaluated using isothermal calorimetry, Thermochim. Acta 546 (2012) 32–43, https://doi.org/10.1016/j.tca.2012.07.010.

[39] V. Kocaba, E. Gallucci, K.L. Scrivener, Methods for determination of degree of reaction of slag in blended cement pastes, Cem. Concr. Res. 42 (2012) 511–525, https://doi.org/10.1016/j.cemconres.2011.11.010.

[40] T. Thoenen, W. Hummel, U. Berner, E. Curti, The PSI/Nagra Chemical Thermodynamic Database 12/07, 2014.

[41] B. Ma, B. Lothenbach, Synthesis, characterization, and thermodynamic study of selected Na-based zeolites, Cem. Concr. Res. 135 (2020) 106111, https://doi.org/10.1016/j.cemconres.2020.106111.

[42] H.C. Helgeson, D.H. Kirkham, G.C. Flowers, Theoretical prediction of the thermodynamic behavior of aqueous electrolytes by high pressures and temperatures; IV, calculation of activity coefficients, osmotic coefficients, and apparent molal and standard and relative partial molal properties to 600 d, Am. J. Sci. 281 (1981) 1249–1516, https://doi.org/10.2475/ajs.281.10.1249.

[43] B.J. Merkel, B. Planer-Friedrich, D.K. Nordstrom, Groundwater Geochemistry: A Practical Guide to Modeling of Natural and Contaminated Aquatic Systems, Springer, 2005.

[44] Y. Zuo, M. Nedeljković, G. Ye, Pore solution composition of alkali-activated slag/fly ash pastes, Cem. Concr. Res. 115 (2019) 230–250, https://doi.org/10.1016/j.cemconres.2018.10.010.

[45] L. Gomez-Zamorano, M. Balonis, B. Erdemli, N. Neithalath, G. Sant, C–(N)–S–H and N–A–S–H gels: compositions and solubility data at 25°C and 50°C, J. Am. Ceram. Soc. 100 (2017) 2700–2711, https://doi.org/10.1111/jace.14715.

[46] E. Bernard, B. Lothenbach, C. Chlique, M. Wyrzykowski, A. Dauzères, I. Pochard, C. Cau-Dit-Coumes, Characterization of magnesium silicate hydrate (M-S-H), Cem. Concr. Res. 116 (2019) 309–330, https://doi.org/10.1016/j.cemconres.2018.09.007.

[47] D. Nied, K. Enemark-Rasmussen, E. L'Hopital, J. Skibsted, B. Lothenbach, Properties of magnesium silicate hydrates (M-S-H), Cem. Concr. Res. 79 (2016) 323–332, https://doi.org/10.1016/j.cemconres.2015.10.003.

[48] A. Fernández-Jiménez, A. Palomo, Composition and microstructure of alkali activated fly ash binder: effect of the activator, Cem. Concr. Res. 35 (2005) 1984–1992, https://doi.org/10.1016/j.cemconres.2005.03.003.

[49] M. Criado, A. Fernández-Jiménez, A.G. de la Torre, M.A.G. Aranda, A. Palomo, An XRD study of the effect of the SiO2/Na2O ratio on the alkali activation of fly ash, Cem. Concr. Res. 37 (2007) 671–679, https://doi.org/10.1016/j.cemconres.2007.01.013.

[50] V. Bocullo, L. Vitola, D. Vaiciukyniene, A. Kantautas, D. Bajare, The influence of the SiO2/Na2O ratio on the low calcium alkali activated binder based on fly ash, Mater. Chem. Phys. 258 (2021) 123846, https://doi.org/10.1016/j.matchemphys.2020.123846.

[51] A.R. Brough, M. Holloway, J. Sykes, A. Atkinson, Sodium silicate-based alkali-activated slag mortars. Part II. The retarding effect of additions of sodium chloride or malic acid, Cem. Concr. Res. 30 (2000) 1375–1379, https://doi.org/10.1016/S0008-8846(00)00356-2.

[52] Z. Sun, A. Vollpracht, Isothermal calorimetry and in-situ XRD study of the NaOH activated fly ash, metakaolin and slag, Cem. Concr. Res. 103 (2018) 110–122, https://doi.org/10.1016/j.cemconres.2017.10.004.

[53] J.A. Gadsden, Infrared Spectra of Minerals and Related Inorganic Compounds, 1975.

[54] M. Criado, A. Fernández-Jiménez, A. Palomo, Alkali activation of fly ash: effect of the SiO2/Na2O ratio. Part I: FTIR study, Microporous Mesoporous Mater. 106 (2007) 180–191, https://doi.org/10.1016/j.micromeso.2007.02.055.

[55] A.A. Hoyos-Montilla, F. Puertas, J. Molina Mosquera, J.I. Tobón, Infrared spectra experimental analyses on alkali-activated fly ash-based binders, Spectrochim. Acta - Part A Mol. Biomol. Spectrosc. 269 (2022) 120698, https://doi.org/10.1016/j.saa.2021.120698.

[56] Y. Yan, S.Y. Yang, G.D. Miron, I.E. Collings, E. L'Hôpital, J. Skibsted, F. Winnefeld, K. Scrivener, B. Lothenbach, Effect of alkali hydroxide on calcium silicate hydrate (C-S-H), Cem. Concr. Res. 151 (2022), https://doi.org/10.1016/j.cemconres.2021.106636.

[57] C. Liu, X. Liang, Y. Chen, Z. Li, G. Ye, Degradation of alkali-activated slag subjected to water immersion, Cem. Concr. Compos. 142 (2023) 105157, https://doi.org/10.1016/j.cemconcomp.2023.105157.

[58] C. Liu, Z. Li, S. Nie, J. Skibsted, G. Ye, Structural evolution of calcium sodium aluminosilicate hydrate (C-(N-)A-S-H) gels induced by water exposure: the impact of Na leaching, Cem. Concr. Res. 178 (2024), https://doi.org/10.1016/j.cemconres.2024.107432.

[59] C.A. Rees, J.L. Provis, G.C. Lukey, J.S.J. Van Deventer, Attenuated total reflectance fourier transform infrared analysis of fly ash geopolymer gel aging, Langmuir 23 (2007) 8170–8179, https://doi.org/10.1021/la700713g.

[60] T. Bakharev, Geopolymeric materials prepared using Class F fly ash and elevated temperature curing, Cem. Concr. Res. 35 (2005) 1224–1232, https://doi.org/10.1016/j.cemconres.2004.06.031.

[61] M. Criado, A. Palomo, A. Fernández-Jiménez, Alkali activation of fly ashes. Part 1: effect of curing conditions on the carbonation of the reaction products, Fuel 84 (2005) 2048–2054, https://doi.org/10.1016/J.FUEL.2005.03.030.

[62] I. García-Lodeiro, A. Fernández-Jiménez, M.T. Blanco, A. Palomo, FTIR study of the sol-gel synthesis of cementitious gels: C-S-H and N-A-S-H, J. Sol-Gel Sci. Technol. 45 (2008) 63–72, https://doi.org/10.1007/s10971-007-1643-6.

[63] F. Winnefeld, A. Leemann, M. Lucuk, P. Svoboda, M. Neuroth, Assessment of phase formation in alkali activated low and high calcium fly ashes in building materials, Constr. Build. Mater. 24 (2010) 1086–1093, https://doi.org/10.1016/j.conbuildmat.2009.11.007.

[64] E. Ul Haq, S.K. Padmanabhan, A. Licciulli, In-situ carbonation of alkali activated fly ash geopolymer, Constr. Build. Mater. 66 (2014) 781–786, https://doi.org/10.1016/j.conbuildmat.2014.06.012.

[65] H. Xu, J.S.J. Van Deventer, The effect of alkali metals on the formation of geopolymeric gels from alkali-feldspars, Colloids Surf. A Physicochem. Eng. Asp. 216 (2003) 27–44, https://doi.org/10.1016/S0927-7757(02)00499-5.

[66] B. Walkley, R. San Nicolas, M.A. Sani, J.D. Gehman, J.S.J. Van Deventer, J. L. Provis, Phase evolution of Na2O-Al2O3-SiO2-H2O gels in synthetic aluminosilicate binders, Dalton Trans. 45 (2016) 5521–5535, https://doi.org/10.1039/c5dt04878h.

[67] E. Ul Haq, S.K. Padmanabhan, A. Licciulli, In-situ carbonation of alkali activated fly ash geopolymer, Constr. Build. Mater. 66 (2014) 781–786, https://doi.org/10.1016/j.conbuildmat.2014.06.012.

[68] S.A. Bernal, J.L. Provis, B. Walkley, R. San Nicolas, J.D. Gehman, D.G. Brice, A. R. Kilcullen, P. Duxson, J.S.J. Van Deventer, Gel nanostructure in alkali-activated binders based on slag and fly ash, and effects of accelerated carbonation, Cem. Concr. Res. 53 (2013) 127–144, https://doi.org/10.1016/j.cemconres.2013.06.007.

[69] M.M. Kumar, H. Jena, Direct single-step synthesis of phase pure zeolite Na–P1, hydroxy sodalite and analcime from coal fly ash and assessment of their Cs+ and Sr2+ removal efficiencies, Microporous Mesoporous Mater. 333 (2022) 111738, https://doi.org/10.1016/j.micromeso.2022.111738.

[70] Y. Ma, J. Hu, G. Ye, The effect of activating solution on the mechanical strength, reaction rate, mineralogy, and microstructure of alkali-activated fly ash, J. Mater. Sci. 47 (2012) 4568–4578, https://doi.org/10.1007/s10853-012-6316-3.

[71] X. Feng, E.J. Garboczi, D.P. Bentz, P.E. Stutzman, T.O. Mason, Estimation of the degree of hydration of blended cement pastes by a scanning electron microscope point-counting procedure, Cem. Concr. Res. 34 (2004) 1787–1793, https://doi.org/10.1016/j.cemconres.2004.01.014.

[72] E. Deir, B.S. Gebregziabiher, S. Peethamparan, Influence of starting material on the early age hydration kinetics, microstructure and composition of binding gel in alkali activated binder systems, Cem. Concr. Compos. 48 (2014) 108–117, https://doi.org/10.1016/j.cemconcomp.2013.11.010.

[73] M.C.G. Juenger, F. Winnefeld, J.L. Provis, J.H. Ideker, Advances in alternative cementitious binders, Cem. Concr. Res. 41 (2011) 1232–1243, https://doi.org/10.1016/j.cemconres.2010.11.012.

[74] Z. Qing, F. Basquiroto, D. Souza, R.J. Mulder, W. Duan, Multistep nucleation and growth mechanism of aluminosilicate gel observed by cryo-electron microscopy, Cem. Concr. Res. 159 (2022) 106873, https://doi.org/10.1016/j.cemconres.2022.106873.

[75] A. Palomo, M.W. Grutzeck, M.T. Blanco, Alkali-activated fly ashes: a cement for the future, Cem. Concr. Res. 29 (1999) 1323–1329, https://doi.org/10.1016/S0008-8846(98)00243-9.

[76] A. Palomo, S. Alonso, A. Fernández-Jiménez, Alkaline activation of fly ashes: NMR study of the reaction products, J. Am. Ceram. Soc. 87 (2004) 1141–1145. https://ceramics.onlinelibrary.wiley.com/doi/pdf/10.1111/j.1551-2916.2004.01141.x. (Accessed 10 May 2019).

[77] G. Fang, M. Zhang, Multiscale micromechanical analysis of alkali-activated fly ash-slag paste, Cem. Concr. Res. 135 (2020) 106141, https://doi.org/10.1016/j.cemconres.2020.106141.

[78] D.G. Bennett, D. Read, M. Atkins, F.P. Glasser, A thermodynamic model for blended cements. II: cement hydrate phases; thermodynamic values and modelling studies, J. Nucl. Mater. 190 (1992) 315–325, https://doi.org/10.1016/0022-3115(92)90096-4.

[79] B. Lothenbach, F. Winnefeld, Thermodynamic modelling of the hydration of Portland cement, Cem. Concr. Res. 36 (2006) 209–226, https://doi.org/10.1016/j.cemconres.2005.03.001.